URTeC: 123

A Collaborative Study on DFIT Interpretation: Integrating Modeling, Field Data, and Analytical Techniques

Mark McClure*[1], Vidya Bammidi[2], Craig Cipolla[3], Dave Cramer[4], Lucas Martin[5], Alexei A Savitski[6], Dave Sobernheim[2], and Kate Voller[7]; 1. ResFrac Corporation, 2. Keane Group, 3. Hess Corporation, 4. ConocoPhillips Company, 5. Formerly with Apache Corporation, now with Marathon Oil Corporation, 6. Shell International Exploration and Production Inc., 7. Range Resources Corporation

Abstract

This paper summarizes findings from a one-year study sponsored by seven operators and service companies to investigate interpretation of diagnostic fracture injection tests (DFIT's). The study combined computational modeling, a diverse collection of field data, and operator experience. DFIT simulations were performed with a three-dimensional hydraulic fracturing, wellbore, and reservoir simulator that describes fracture propagation, contacting of the fracture walls, and multiphase flow. Interpretation procedures were applied to estimate stress, permeability, and pressure from the synthetic data. The interpretations were compared to the simulation input parameters to evaluate accuracy. Based on the results, new techniques were developed, existing techniques were refined, and an overall interpretation protocol was developed. The techniques were applied to interpret over thirty field DFIT's drawn from shale plays across the US and Canada, and the methods were evaluated in the context of operator experience. The results are applicable to fracturing tests in formations with permeability ranging from nanodarcies to 10s of microdarcies. The minimum principal stress is estimated by identifying the 'contact pressure' when the fracture walls come into contact, causing fracture compliance and system storage coefficient to decrease. After the walls come into contact, the pressure transient is controlled by the interplay of changing fracture compliance, deviation from Carter leakoff, and multiphase flow. The contact pressure is slightly greater than the minimum principal stress. It can be identified from either a plot of dP/dG or a relative stiffness plot. Permeability is estimated using the G-function method, a newly developed h-function method that accounts for deviation from Carter leakoff, and impulse linear flow. These three methods, which are based on linear flow geometry, require an estimate of fracture area. We derive equations for estimating area using mass balance equations, accounting for wellbore storage and fluid leakoff. The results from field data show that impulse linear permeability estimates are usually 2-5 times lower than estimates derived from the G-function and h-function methods, apparently indicating a difference between effective permeability during leakoff and permeability during flow of reservoir fluid through the formation. Impulse radial flow regime may be used for estimating permeability, but should be used with caution. Simulation results indicate that a variety of processes can cause an apparent radial trend that is not actually radial flow. Simulations and field data indicate that 'false radial' is very common in gas reservoirs and, if applied, leads to a large overestimate of permeability. Production history matching using overestimated permeability will underestimate fracture length, potentially resulting in suboptimal choices for well and cluster spacing.

1. Introduction

1.1 Background

Diagnostic fracture injection tests (DFIT's) involve water injection at a rate and pressure sufficient to create a dominant hydraulic fracture, followed by a shut-in period lasting days, weeks, or even months. The trend in pressure after shut-in is analyzed to estimate stress, permeability, and/or pore pressure. Compared with other types of fracture injection tests, DFIT's typically involve a longer shut-in, are performed after drilling is complete, are usually performed in low permeability rock, and have a greater emphasis on estimating reservoir properties, such as permeability and pore pressure.

The magnitude of the minimum principal stress, permeability, and pore pressure are key parameters in reservoir engineering, hydraulic fracturing, and drilling. Knowledge of the stress state is used during drilling (wellbore stability and mitigation of lost circulation), exploration (fault seal analysis and prediction of critically stressed fractures), and hydraulic fracturing (predicting injection pressure, estimating height growth, selecting proppant, and inferring net pressure) (Zoback, 2007; Economides and Nolte, 2000; Smith and Montgomery, 2015). Permeability estimates are used during optimization of hydraulic fracture design, well spacing, and cluster spacing. Pore pressure estimates are used to delineate the extent of drainage, which helps with optimization of well spacing.

Permeability is difficult to measure in unconventional formations. Permeability from core may not be directly applicable in reservoir engineering calculations because in-situ flow can be strongly influenced by pre-existing planes of weakness that are not sampled in the core. In addition, core measurement may be impacted by changes in the rock as it is removed from the subsurface. Rate-transient analysis (RTA) yields an estimate of fracture surface area times the square root of permeability ($A\sqrt{k}$), but cannot estimate these parameters separately. On the other hand, DFIT's provide the opportunity to derive a unique, in-situ estimate of permeability. The DFIT provides a permeability estimate that is the area-weighted average of the permeability across the fracture surface area. It is an estimate of the effective permeability to the mobile reservoir phase (absolute permeability times relative permeability).

This paper summarizes findings from a one-year study sponsored by seven operators and service companies. The purpose of the study was to evaluate the accuracy of existing DFIT interpretation techniques, develop new techniques if needed, and assemble an overall interpretation procedure. The study integrated unique simulation capability, field data, and operator expertise. The interpretation procedure can be performed entirely in an Excel spreadsheet.

The body of the paper presents a step-by-step worked example, commentary on the most important findings, and additional field examples. The appendix provides detailed mathematical derivations explaining the methods applied in the paper

The study focused primarily on DFIT's performed in formations with permeability on the order of nanodarcies to 10s of microdarcies. With higher permeability, transients behave qualitatively differently, and many of the techniques in this paper cannot be applied (discussed in Section 4.1).

1.2 Literature review

DFIT interpretation combines concepts from well test analysis and hydraulic fracture analysis. Conventional well testing involves production or injection of fluid at pressure below the fracture gradient. Pressure data is analyzed to infer permeability, skin, and other parameters (Theis, 1935; Horne, 1995; Kamal et al., 2009; Stewart, 2011; Spivey and Lee, 2013). DFIT's involve similar physics, but with important differences. In conventional well tests, fractures are static. In DFIT's, fractures are dynamic – changing in size, compliance, and conductivity. As a result, concepts from conventional well test analysis are not always directly applicable to DFIT analysis.

Hydraulic fracturing was first described in a publication by Clark (1949). In subsequent decades, it was recognized that hydraulic fracturing could be used as a method to estimate the magnitude of the minimum

principal stress (Hubbert and Willis, 1957; Godbey and Hodges, 1958; Kehle, 1964; Haimson and Fairhurst, 1967; Hickman and Zoback, 1983). If fluid is injected at pressure greater than the minimum principal stress, a hydraulic fracture will form and propagate through the formation. As a result, the minimum principal stress can be estimated from pressure measurements during and after injection (Economides and Nolte, 2000; Zoback, 2007; Smith and Montgomery, 2015). The uniaxial stress/strain equations can be used for engineering purposes to help predict stress differences between layers (Eaton, 1969; Blanton and Olson, 1999), but fracture injection tests are needed for calibration and to ensure accuracy.

Nolte (1979) extended the applicability of fracturing tests by developing analytical techniques that can be used to estimate fluid leakoff parameters. These techniques can assess leakoff even when using complex fluids that develop filtercake. These tests are typically called minifrac tests (McLennan and Roegiers, 1982) or fracture calibration tests (Mayerhofer and Economides, 1993). The G-function developed by Nolte (1979) became a routine part of data plotting and interpretation (Castillo, 1987; Barree and Mukherjee, 1996). Mayerhofer and Economides (1993) and Mayerhofer et al. (1995) showed how to disentangle the effects of filtercake and formation permeability on leakoff.

Conventional well testing is infeasible in very tight formations because of the difficulty of sustaining sufficiently low rates of production or injection. The "diagnostic fracture injection test" (DFIT) emerged to combine the benefits of a well test and a fracturing test – providing estimates for stress, permeability, and pore pressure (Craig and Brown, 1999). 'Preclosure' analysis methods are usually based on techniques from Nolte (1979) and Mayerhofer and Economides (1993) and Mayerhofer et al. (1995). Barree and Mukherjee (1996) and Barree et al. (2009) developed techniques for qualitative interpretation and for estimating the closure pressure and minimum principal stress. Impulse analysis is based on the use of impulse solutions from conventional well testing (Gu et al., 1993; Soliman et al., 2005; Craig and Blasingame, 2006) or the 'linear flow time function' technique developed by Nolte et al. (1997). Examples of DFIT interpretation are provided in recent papers by Marongiu-Porcu et al. (2011; 2014), Soliman and Kabir (2012), Soliman and Gamadi (2012), Cramer and Nguyen (2013), Padmakar (2013), Wallace et al. (2014), Meng et al. (2014), Craig (2014), Zanganeh et al. (2018), and Hawkes et al. (2018).

McClure et al. (2014; 2016) and Jung et al. (2016) proposed the compliance method of estimating stress from a DFIT (Section 3.1.2). The compliance method leads to an earlier, higher stress estimate than the commonly used tangent method (Barree et al., 2009). McClure et al. (2016) and Jung et al. (2016) performed detailed DFIT simulations considering the effect of residual aperture fracture after the fracture walls contact. Simulations indicate that in low permeability formations, the contacting of the fracture walls causes the magnitude of the pressure derivative to increase, resulting in a pressure signal often interpreted as height recession or closure of transverse fractures (Barree et al., 2009). Wang and Sharma (2017) reproduced these findings and proposed a modified approach for estimating stress called the 'variable compliance method.'

1.3 Defining a new term – the 'contact pressure'

The term 'closure pressure' is used widely in the literature but is rarely given a precise definition. A review of the literature shows that a variety of assumptions are made about 'closure pressure,' and these assumptions are often problematic and inconsistent. Most authors assume that the closure pressure is equal to the magnitude of the minimum principal stress (issues with this definition are discussed in Section A.2). Craig and Blasingame (2006) assume that the compliance (or compressibility) of a 'closed' fracture is negligible (issues with this definition are discussed in Section A.2). The classical calculation of efficiency from the G-time to closure (Equation 5) is derived assuming that there is zero fluid remaining in the fracture at 'closure' (issues with this assumption are discussed in Section A.12). McClure et al. (2016) define closure as being the point in time when the fracture walls first come into contact, decreasing the overall compliance of the system (issues with this definition are discussed in Section 3.1.9). Nolte et al. (1997) derive the 'linear flow time function' assuming that Carter leakoff occurs until closure, at which point leakoff rate drops to zero (issues with this definition are discussed in Section A.11).

In Section A.2, we show that there is not any specific response in the pressure transient (or any other measurement) when fluid pressure is exactly equal to the minimum principal stress, Shmin. Instead, Shmin can be estimated from its proximity to a process that does create a signature in the pressure transient – the contacting of the fracture walls, which causes a measurable increase in the system stiffness (or decrease in compliance). We define the pressure at this point in time as the 'contact pressure.' It is equivalent to the 'closure pressure' defined by McClure et al. (2016). However, because the definition of 'closure pressure' is itself a point of confusion, we prefer to use the term 'contact pressure.'

1.4 Study approach

In our study, we performed a comprehensive reassessment of the entire DFIT analysis procedure – estimating stress, permeability, and pore pressure. Based on the results, we developed a detailed, step-by-step interpretation procedure.

First, a large number of DFIT simulations were performed under a variety of conditions. The simulations were performed with a three-dimensional hydraulic fracturing, wellbore, and reservoir simulator that rigorously handles fracture propagation, contacting of the fracture walls, and multiphase flow (McClure and Kang, 2018). Conventionally, DFIT simulations and/or analytical approaches have isolated parts of the problem and solved them separately. The fully integrated approach used in this study captures the interactions between processes, which have a material impact on system behavior.

Different analysis procedures were applied to analyze the simulations results, and the interpretations were compared with the (known) simulation input parameters to assess accuracy. Based on the results, a set of DFIT interpretation guidelines were developed (summarized in Section 2.2). The guidelines incorporate both pre-existing methods and newly developed techniques.

The interpretation guidelines were applied to analyze a dataset of field DFIT's contributed by operators. The results were compared with operator experience and expertise to assess performance. Due to limits on paper length, only a small set of the simulations and the field results are shared in this paper.

This paper does not address many operational aspects of performing DFIT's. Cramer and Nguyen (2013) review practical guidelines for DFIT execution.

2. Methods

2.1 Numerical simulator

Numerical simulations were performed using ResFrac, a three-dimensional hydraulic fracturing, reservoir, and wellbore simulator. The problem formulation is briefly summarized in this section, and a detailed technical description is provided by McClure and Kang (2018). ResFrac has a unique combination of physics that enables seamless description of the entire DFIT process, from the beginning of injection to late-time impulse flow. The wellbore is meshed from the surface as a series of line-segments. The fracture is meshed with rectangles, and the reservoir is meshed with cuboids.

The unsteady-state mass balance equation is solved in every element at every timestep. Multiphase flow is described with the black oil model or the compositional model. Fracture walls come out of contact when fluid pressure exceeds normal stress. Then, the amount of mechanical opening in each element is calculated to enforce that the fluid pressure is equal to the normal stress on the element, including stress shadow effects from all other mechanically open elements. The stress interaction is calculated with the 3D displacement discontinuity method of Shou et al. (1997), an approach that provides mesh convergent solutions identical to classical continuum mechanics solutions, such as from Sneddon (1946). The opening of every fracture element affects the stress on every other element, requiring the solution of a large, coupled system of equations in every timestep.

When the fluid pressure drops sufficiently, the fracture walls come into contact. After the walls contact, the elements retain aperture and the ability to conduct fluid. The aperture is calculated using the Willis-Richards

et al. (1996) version of the Barton et al. (1985) relations. This joint closure law implicitly handles the contacting of the asperities in the fracture walls (Barton et al., 1985; Willis-Richards et al., 1996):

$$W = \frac{W_0}{1+\frac{9(\sigma_n - P)}{\sigma_{n,ref}}}. \quad (1)$$

The W_0 parameter (Equation 1) corresponds to the average fracture aperture at the contact pressure – the pressure when asperities begin to contact, the fracture stiffens, and normal stress is transferred across the fracture by solid-solid contact. Conductivity is calculated with the cubic law (Witherspoon et al., 1980).

Even as the average fracture aperture remains above zero, it is implicit to Equation 1 that the fracture walls are in contact across a fraction of the fracture area, at a scale below the resolution of the model (Barton et al., 1985). Some numerical modeling approaches explicitly represent individual asperities (Vogler et al., 2018). However, this approach is computationally expensive and infeasible for field-scale modeling.

When a new fracture element is created in the model, it is given a very low initial aperture, 1 micron. The aperture when the walls contact, W_0, cannot initially exceed this initial aperture, and so as the crack opens, W_0 must increase along with aperture to reach a more physically realistic value. W_0 is increased at the end of each timestep to be equal to a certain fraction of the total aperture, up to a user-specified limit, $W_{0,max}$. This corresponds to a progressive process of crack formation – roughness developing as the crack transitions from 'not-yet-formed' to 'fully formed.' In reality, this process is controlled by the rock fabric (Suarez-Rivera et al., 2013; Gale et al., 2018), is probably scale-dependent (Delaney et al., 1986; Scholz, 2010), and might depend on operational parameters such as injection rate. After the walls have come into contact, aperture has decreased by 90% once effective normal stress reaches $\sigma_{n,ref}$.

The wellbore model solves the momentum balance equation in each element (in addition to the mass balance equations) and includes hydrostatic head, friction, momentum accumulation, and pressure gradient. Flow between well elements and fracture elements includes the effect of pressure drop due to both perforation (scaling with the square of flow rate) and near-wellbore pressure drop (Equation 22).

Poroelastic stress changes are rarely considered in DFIT analysis and were not included in the simulations performed for this study. In low permeability formations, the region of pressure increase around the fracture will be very narrow. As a result, the poroelastic increase on fracture normal stress will be small (Perkins and Gonzalez, 1985). Nevertheless, it cannot be assumed that poroelastic stresses will never have a significant impact, and this would be an interesting topic for further study.

2.2 Interpretation procedure

An interpretation procedure was developed based on simulation results, analytical derivations, and application to field data. The procedure is:

(1) Inspect a plot of pressure versus time to pick the start of injection and the shut-in time. The pressure plot should be used to pick shut-in because injection rate data is often unavailable or not synchronized with the pressure data.

(2) Smooth the shut-in pressure transient by resampling along pressure increments (Horne, 1995). A 30 psi increment usually yields good results.

(3) Construct plots of the shut-in data: dP/dG versus G (Section A.3) and a log-log plot of dP and t*dP/dt (using actual shut-in time, not superposition time; McClure, 2017). Depending on the interpretation, plots of pressure versus t^-1 and t^(-1/2) may also be used. According to the interpreter's preference, other plots can be constructed (G*dP/dG, a log-log plot with the primary derivative dP/dt, linear-flow time function, etc.).

(4) Estimate the wellbore storage coefficient from a plot of cumulative volume injected versus pressure prior to breakdown.

(5) Identify the point of minimum dP/dG prior to the contact pressure and extrapolate back to G-time equal to zero to estimate the effective ISIP (Section 3.1.1). Calculate the 'effective pressure' curve, defined as being equal to measured pressure after the minimum dP/dG and equal to the linear extrapolation of pressure prior to dP/dG (Section 3.1.1). Section 4.1 discusses interpretation of tests with monotonically decreasing dP/dG.

(6) Construct an afterflow plot to assess near-wellbore pressure drop (Sections 3.1.4 and A.7).

(7) From the log-log plot, identify impulse linear or radial flow regimes from a -1/2 or -1 slope. Be cautious about identification of these flow-regime trends (Section 3.1.5). Do not use the log-log plot for interpretation prior to the late-time impulse period (ie, prior to the peak in t*dP/dt).

(8) Depending on the diagnosis of impulse flow, estimate pore pressure from plots of pressure versus either t^-1 or t^(-1/2) (Sections 3.1.6 and A.6). If an unambiguous diagnosis of impulse flow is not possible, consider reducing injection volume to accelerate the onset of impulse flow in subsequent tests. It is possible to perform an extrapolation of the t^(-1/2) or t^(-1) plot, even in the absence of a clear straight line. This strategy should be used with caution because it can be significantly inaccurate. Section A.13 outlines an alternative technique that can be used with short-duration transients.

(9) Calculate the h-function (Section A.8) and construct a plot of h-function versus G-function and a relative stiffness plot (Sections 3.1.2 and A.9).

(10) Using the dP/dG curve and the relative stiffness plot, identify the contact pressure and estimate the magnitude of the minimum principal stress (Section 3.1.2). Section 4.1 discusses interpretation of tests where the contact pressure cannot be identified.

(11) Estimate permeability (Section 3.1.7) using the G-function method (Section A.10.i), the h-function method (Section A.10.ii), and (if applicable) impulse linear or radial (Sections A.10.iii and A.10.iv). Compare the results and check for consistency. Keep in mind that impulse linear estimates are usually 2-5 times lower than estimates from the other methods. The impulse linear estimate is probably the most applicable for predictions of production, and so a downward adjustment may be warranted if an impulse linear permeability estimate is not available.

(12) Optionally, create a plot of estimated aperture versus effective normal stress (Sections 3.1.9 and A.14).

In advance of a test, it is often useful to estimate the duration of shut-in needed to reach impulse flow. This could be done by performing a numerical simulation with code such as ResFrac (McClure and Kang, 2018) or by performing a simplified DFIT simulation using the equations in Section A.13. DFIT simulations may be performed after the interpretation as a quality control to confirm that the simulation result is consistent with the actual data.

3. Results

3.1 Example interpretation

The interpretation procedure is demonstrated in the following example using a DFIT performed in a gas well in the Utica/Point Pleasant. Mathematical background is provided in the appendix. It may be useful to refer to the appendix while reading this section.

3.1.1 Initial interpretation with the G-function plot

Figure 1 shows a plot of pressure and dP/dG versus G-time. For convenience, dP/dG is plotted as positive, even though it is actually negative (because pressure is decreasing over time).

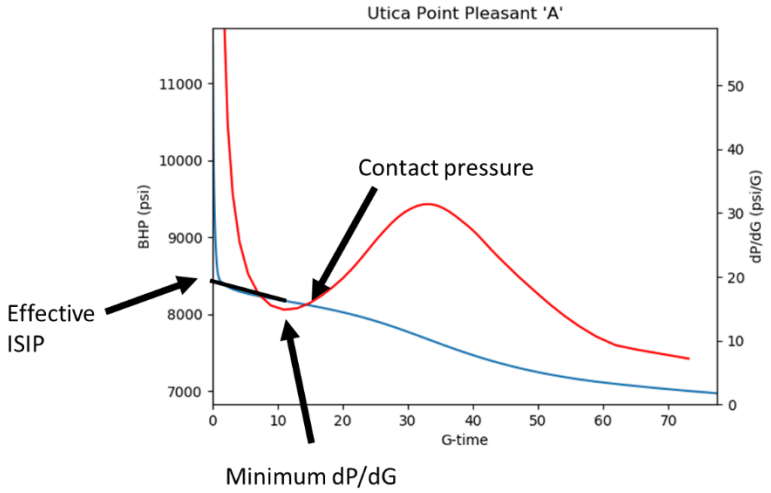

Figure 1: dP/dG and pressure versus G-time for the Utica DFIT.

Ideally, dP/dG should be constant as long as the fracture walls are out of contact (Nolte, 1979; Castillo, 1987; Section A.3). However, this is not usually observed in field DFIT's, especially if performed in a horizontal well.

At early time, the pressure derivative is elevated by near-wellbore pressure drop. The near-wellbore pressure drop is caused by flow through a tortuous path through the cement sheath and axial (longitudinal) fractures in the near-wellbore region (Wright, 2000; Weijers et al., 2002; Economides and Martin, 2008; Bazan and Meyer, 2015; Cramer et al., 2019). Because of this pressure drop, the pressure in the primary fracture away from the well is lower than the pressure measured in the wellbore (Figure 2). Some authors distinguish between 'near-field' and 'mid-field' pressure drop, but in this paper, we lump these processes together and refer to them as simply 'near-wellbore pressure drop.'

In Figure 1, the literal ISIP is around 11,500 psi. The effective ISIP, 8330 psi, is estimated by identifying the point of minimum dP/dG and extrapolating the pressure versus G-time curve back to zero from this point. The effective ISIP is an estimate for the pressure in the far-field fracture at shut-in. This is the pressure actually present in the fracture that is opening and propagating the crack.

Figure 2 illustrates the difference between literal ISIP and effective ISIP. A fracture is shown initiating longitudinally along the well. Away from the well, a transverse fracture forms, resulting in a complex, tortuous fracture geometry that causes a substantial pressure drop that takes at least several minutes to dissipate. Figures 13 and 17 from Jung et al. (2016) show numerical simulations of this process.

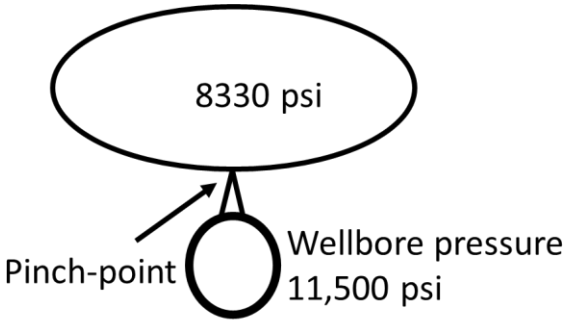

Figure 2: Schematic of near-wellbore pressure drop between the wellbore and the far-field fracture.

As the fracture walls come into contact, the magnitude of the pressure derivative begins to increase as the fracture compliance and system storage coefficient decrease because of the contact stress (McClure et al.,

2016; Section A.2). The point of minimum dP/dG is closest to the 'true' dP/dG in the far-field fracture because it is least disturbed by near-wellbore pressure drop and the contacting of the fracture walls.

The 'effective pressure' is defined as being equal to measured pressure after the point of minimum dP/dG, and equal to the linear extrapolation of pressure back to G-time equal to zero prior to the point of minimum dP/dG (Figure 1). Effective pressure is an estimate for the pressure that is actually in the fracture. As shown in Figure 2, the pressure measured in the well is higher than the 'effective pressure' because of the pressure drop that occurs between the well and the far-field fracture.

Conventionally, a period of rapid pressure drop after shut-in has been called 'tip-extension' or 'pressure-dependent leakoff' (PDL). It has been believed to be caused by accelerated leakoff or pressure gradient along the fracture or at the tip (Barree et al., 2009; Liu et al., 2016). However, it has also been recognized that near-wellbore fracture tortuosity is responsible for the huge pressure drops observed after shut-in (Bazan and Meyer, 2015; McClure et al., 2016; Barree and Miskimins, 2016). The distinction is that in the 'near-wellbore pressure drop' interpretation, the pressure in the fracture is much lower than the literal ISIP (the bottomhole pressure very shortly after shut-in), but in a 'tip-extension' or 'PDL' interpretation, the pressure in the fracture is close to the literal ISIP.

As pressure drops after shut-in, a few barrels of water will be released from wellbore storage and cause a limited amount of tip-extension. If pressure-dependent leakoff is taking place, it will be impossible to observe because of the huge pressure changes caused by the dissipation of near-wellbore pressure drop. Therefore, while PDL and tip-extension may occur, 'near-wellbore pressure drop' is the dominant physical process in most DFIT's and should be considered the primary interpretation.

In vertical wells, the pressure drop after shut-in is usually (though not always) less pronounced than in horizontal wells (Section 3.3). This is consistent with the interpretation that near-wellbore pressure drop is the primary cause of the large pressure drops observed after shut-in, and this process is related to fracture tortuosity due to fracture reorientation.

3.1.2 Estimating the minimum principal stress

As described by McClure et al. (2016) and in Section A.2, the fracture compliance begins to decrease after the fracture walls come into contact. The decreasing fracture compliance causes the pressure to drop more rapidly (the magnitude of dP/dG increases). McClure et al. (2016) recommend picking the contact pressure from a G*dP/dG plot. However, there is not always a unique feature on the G*dP/dG plot that lends itself to identifying the contact pressure. It is better to pick the contact pressure from a plot of dP/dG. The contact pressure occurs when dP/dG begins to increase from its minimum value. A rule of thumb is to pick the contact pressure when there has been a 10% increase from the minimum. When constructing a dP/dG plot, the y-axis scale should be chosen so that the minimum and maximum dP/dG can be clearly observed. Large early time dP/dG values do not need to be visible on the plot and can go up off the scale. They are related to dissipative processes unrelated to fracture contact (Section 3.1.1).

As explained in Section A.2, the contact pressure is slightly above the minimum principal stress. In simulations that match field pressure data, we have found that subtracting approximately 75 psi from the contact pressure is a good rule-of-thumb for providing a good estimate of Shmin. However, this is a source of uncertainty and is an inherent limitation to stress estimation from fracturing data. As discussed in Section A.2, there is not any response in the pressure transient when pressure is actually equal to Shmin. It is known that the contact pressure is close to Shmin (and slightly larger), and so stress can be estimated by identifying the contact pressure and then making a small downward adjustment to reach Shmin.

The G-function is derived assuming Carter leakoff, which is strictly valid only if fluid pressure in the fracture is constant over time. As pressure decreases during shut-in, deviation from Carter leakoff occurs, causing leakoff to occur more slowly than anticipated by the G-function. This overprints a tendency for dP/dG to decrease. Ultimately, decreasing leakoff rate is the reason that dP/dG decreases asymptotically to zero at late time.

Fracture contact causes dP/dG to increase, and deviation from Carter leakoff causes dP/dG to decrease. If fracture contact occurs simultaneously with deviation from Carter leakoff, the effects could offset and mask the effect of contact on the transient. The problem becomes more significant when effective ISIP minus Shmin (net pressure) is a substantial fraction of effective ISIP minus pore pressure. The practical consequence is that contact causes a stronger dP/dG response in formations where Shmin and pore pressure are relatively further apart.

In an extreme case, Craig et al. (2017) attempted to estimate stress using a G-function plot of pressure from laboratory experiment in which ISIP was double the magnitude of the minimum principal stress (and near-wellbore pressure drop was negligible). Because net pressure was so large relative to ISIP minus pore pressure, by the time that pressure reached the minimum principal stress, the overprint of deviation from Carter leakoff was very strong, and a G-function interpretation of the data was not meaningful.

To solve this problem, a relative stiffness plot can be used to identify the contact pressure, even in cases where there is substantial deviation from Carter leakoff (Wang and Sharma, 2018; Section A.9). The plot can be constructed solely from the pressure data and an estimate of pore pressure. The plot shows relative changes in system stiffness (or storage coefficient) and rigorously accounts for the impact of pressure change in the fracture on leakoff rate.

Figure 3 shows that in the example dataset, there is a distinct increase in relative stiffness at around 8100 psi. This corresponds to the point in the G-function plot when dP/dG begins to increase from the minimum. The Shmin estimate is 8100 – 75 = 8025 psi.

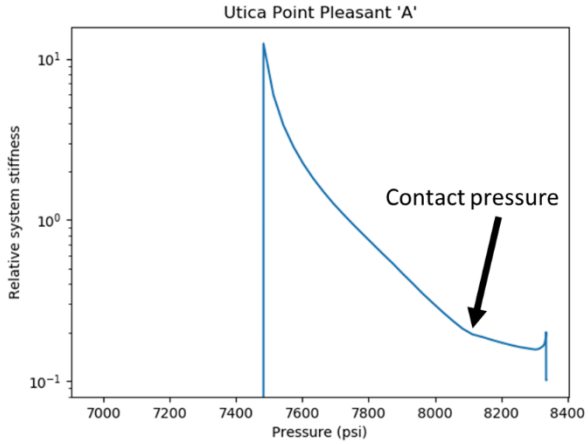

Figure 3: Relative stiffness plot of the Utica DFIT.

3.1.3 Difference with conventional interpretation

Conventionally, Shmin has been estimated from plots of G*dP/dG versus G-time, by drawing a line from the origin to the tangent to G*dP/dG (Barree et al., 2009). This technique does not have theoretical or mathematical justification and yields an inaccurate stress estimate when applied to numerical simulations that realistically capture nonlinear evolving fracture stiffness after contact (McClure et al., 2014; 2016). Craig et al. (2017) claim to use field and laboratory data to validate the tangent method. McClure (2019) describes technical and methodological problems with this study.

The tangent to G*dP/dG tends to occur very close to the peak in G*dP/dG. It can be shown mathematically that the peak in G*dP/dG occurs at the same time as the peak in t*dP/dt. The peak in t*dP/dt has a physical meaning – it corresponds to the transition from Carter leakoff to late-time impulse flow (McClure, 2017). The timing of the transition is strongly affected by the formation fluid pressure (McClure, 2017). We performed sensitivity analysis simulations varying pore pressure and holding Shmin constant. The simulations showed that as pore pressure was decreased, the tangent method estimate of Shmin decreased

(even though Shmin was being held constant in the simulations). The implication is that the tangent method underestimates Shmin more significantly in formations with greater difference between Shmin and pore pressure.

For the DFIT shown in Figure 1, the tangent method (applied to a plot of G*dP/dG) yields a stress estimate of 7633 psi, about 400 psi lower than the estimate presented in Section 3.1.2. The implied net pressure from the tangent method is nearly triple, implying a much shorter, wider fracture.

The phenomenon of increasing dP/dG during shut-in (causing a concave up trend on a plot of G*dP/dG) has conventionally been ascribed to 'fracture height recession' or 'closure of transverse fractures' (Barree et al., 2009). Jung et al. (2016) performed detailed simulations of these processes. The simulations showed that these processes have a second-order effect and cause, at most, minor uncertainty in the stress estimate. The bulk of the increase in dP/dG occurs after the fracture walls have come into contact across the entire fracture area.

Some investigators have recently speculated that the contact pressure might be interpreted as the 'start of closure' and the tangent method pick might be interpreted as the 'end of closure.' This interpretation is not supported by our modeling results. Simulations show that the great majority of increase in system stiffness and dP/dG occurs after contact has occurred along the entire fracture area, and this occurs at a pressure substantially higher than the tangent pick. This was observed in simulations performed by McClure et al. (2016) and was also observed in the simulations performed for this study.

3.1.4 Afterflow plot

Using the estimate of effective ISIP, it is possible to construct an afterflow plot showing the relationship between flow rate from the well after shut-in and the pressure difference between the well and the far-field fracture (Section A.7).

Figure 4 shows the afterflow plot for the Utica DFIT. The relationship is well-described by a square root curve, consistent with relations proposed in the literature (Equation 22; Wright, 2000). In Figure 4, data from the first 15 seconds after shut-in is not shown because it is complicated by water hammer and perforation pressure drop. From visual inspection of Figure 4, the near-wellbore coefficient (Equation 22) is approximately 1600 psi/bpm^(1/2). Square root scaling of afterflow was observed in the great majority of the field DFIT's reviewed in this study.

Sometimes, DFIT's are performed with a rate step-down at the end of injection. This is not necessary because an afterflow plot can be used to extract information regarding the near-wellbore pressure drop without performing a step-down.

The near-wellbore pressure drop observed in a DFIT is typically much larger than in field-scale fracturing treatments because the tortuous path is scoured out by proppant, acid spearhead, and fracture development from progressive injection (Cramer et al., 2019).

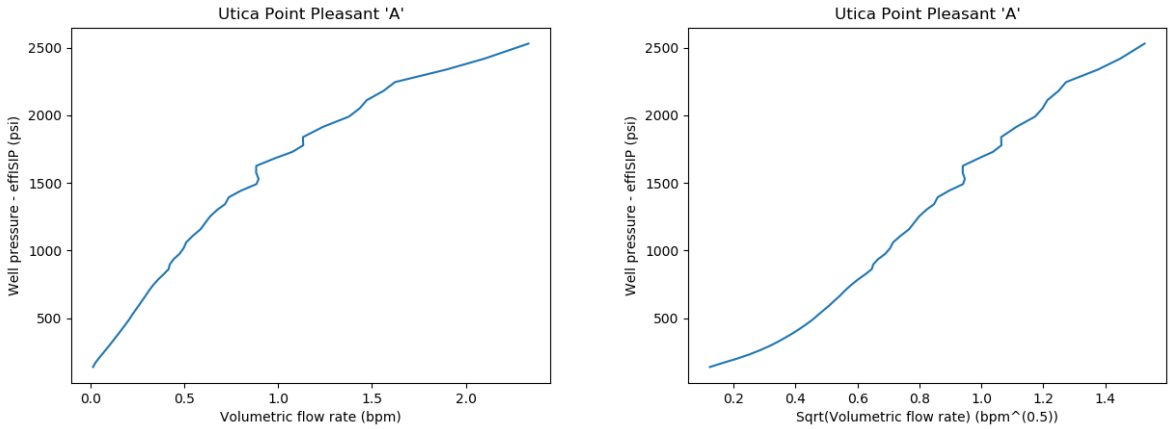

Figure 4: Afterflow plots for the Utica DFIT.

3.1.5 Diagnosing impulse transients

Figure 5 shows a log-log plot of the data. The t*dP/dt curve has the useful property that if $\Delta P \propto t^{\alpha}$, then the slope of the curve is equal to α (Bourdet et al., 1983). The derivative is taken with respect to actual shut-in time. Sometimes, log-log derivative plots are calculated with superposition time, rather than actual shut-in time (Marongiu-Porcu et al., 2011, 2014; Liu et al., 2016). This technique is useful for conventional well tests, but is unnecessary for interpretation of DFIT's (McClure, 2017).

In a DFIT, the log-log plot should only be used to interpret the late-time transient behavior that occurs after the hump in t*dP/dt (which occurs at 2000 min in Figure 5). The log-log plot should not be used to interpret the transient prior to the hump in t*dP/dt. For example, the derivative curve in Figure 5 is approximately flat from about 20 to 200 minutes In a conventional well test, this trend would be interpreted as being radial flow. However, the physics of a DFIT are different from a conventional well test, and radial flow from 20 to 200 min is not the correct interpretation.

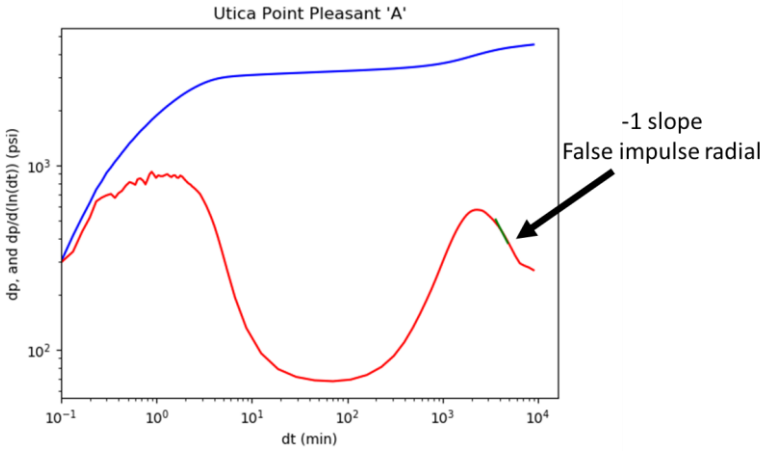

Figure 5: Log-log plot for a Utica DFIT. Derivative is taken with respect to actual shut-in time.

The transient following the hump in t*dP/dt can be described mathematically as an 'impulse' test in which a volume of fluid is instantaneously injected and then the fluid spreads out and pressure asymptotically returns to the initial pressure (Gu et al., 1993; Craig and Blasingame, 2006; McClure, 2017). Impulse linear behavior scales with t^(-1/2) (a -1/2 slope on the log-log plot), and impulse radial scales with t^-1 (a -1 slope on the log-log plot).

Figure 5 shows that soon after the peak in t*dP/dt, the transient rolls over into a -1 slope. It is tempting to identify this trend as impulse radial flow. However, our simulation results suggest that this apparent radial signature should be interpreted as 'false radial' – a transient that exhibits t^-1 scaling, but which is not actually radial flow. We observed this phenomenon in every simulation that we performed of a DFIT in a gas reservoir. The anomalously rapid pressure drop apparently arises from interaction between several effects: viscosity contrast between the injection fluid and the gas in the formation, evolving fracture stiffness after contact, and the transition from Carter leakoff to impulse flow. In examination of field data from gas DFIT's in the Utica, Marcellus, and Montney, a rolling over from the peak t*dP/dt into an approximately -1 slope (without an intervening -1/2 slope) was observed in the majority of cases.

Simulations predict that if shut-in is performed long enough, the transient settles into a -1/2 slope after the -1 slope. This was observed in one of the DFIT's reviewed in this study, which had an unusually long shut-in after the peak in t*dP/dG. The -1 slope represents a period of transition from the hump in t*dP/dt to an eventual -1/2 slope that indicates linear flow. Because of the low viscosity of the reservoir fluid, the location of the -1/2 slope on the log-log plot tends to be significantly lower than the hump in t*dP/dt. Therefore, the curve temporarily steepens as it transitions from the peak t*dP/dt to the late-time impulse trend.

Genuine impulse radial is most likely to be seen in smaller volume tests (<15 bbl) and if permeability divided by viscosity is greater than 1 microdarcy/cp.

In DFIT simulations performed in water saturated or oil saturated formations, the baseline behavior was for the transient to roll over into a -1/2 slope, as expected for linear flow. However, sensitivity analysis simulations suggest that a variety of non-ideal processes may cause anomalous late-time behavior. In simulations performed with multiple closely spaced fractures, pressure interference between the fractures caused a variety of different trends after the hump in t*dP/dt, including a false radial trend. Simulations suggest that dual porosity behavior in the surrounding reservoir (either pseudosteady state or transient) may cause a false radial signature. In real data, a variety of unusual behaviors can be seen in late-time data. We do not attempt to interpret these signatures because of there is not enough information to differentiate between different possible interpretations. Because of these issues, impulse permeability estimates should be compared with the results from the h-function and G-function methods, and if there is large discrepancy, the results should be regarded with lower confidence. Performing multiple DFIT's in the same formation in different wells is a good way to test for consistency and identify anomalous results.

Zanganeh et al. (2018) also performed simulations suggesting the possibility of false radial flow after the peak in t*dP/dt. However, their simulations did not consider multiphase effects or multiple fracture strands. Our findings are different because under the basic conditions of one fracture strand and single phase flow, we did not observe false radial. The cause of the discrepancy is unclear, but may be related to how they modeled fracture compliance evolution as the fracture closed.

Finally, interpreters should keep in mind that poroelastic responses caused by injection or production activity in offset wells can occur at substantial distances, causing abrupt and anomalous responses. These responses are most likely to affect late-time transients because they have the greatest duration and are sensitive to small pressure changes.

3.1.6 Pore pressure estimation

The pore pressure can be estimated by linearly extrapolating the pressure trend during impulse flow to reciprocal time (or reciprocal square root time) of zero (Section A.6). Extrapolation of the pressure trend in Figure 6 yields a pressure estimate of 6825 psi. As discussed in Section 3.1.5, the straight line in Figure 6 is not actually radial flow. If the transient had extended for much longer, the derivative curve would have likely straightened into a linear signature (resulting in a more rapid decrease in pressure than if the trend had continued along a t^-1 scaling). Therefore, pore pressure is probably modestly lower than 6825 psi.

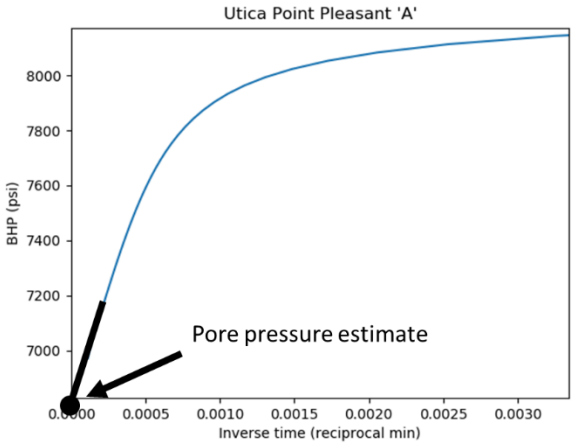

Figure 6: Pressure versus reciprocal time for a Utica DFIT.

3.1.7 Permeability estimation from linear flow transients

Permeability can be estimated using three linear-flow techniques (G-function, h-function, and impulse linear) and from impulse radial-flow. In the example transient, impulse linear is not apparent and so cannot be used.

The G-function method calculates leakoff coefficient from dP/dG, and permeability is calculated from leakoff coefficient (Nolte, 1979; Valko and Economides, 1999; Section A.10.i). However, in the example dataset, dP/dG is constantly changing (Figure 1). Which value of dP/dG should be used? As discussed in Section 3.1.1, the minimum dP/dG is the point least disturbed by either near-wellbore pressure drop or contacting of the fracture walls. Therefore, this is the point that is most representative of the true value of dP/dG in the fracture, and it should be used to estimate leakoff coefficient.

The calculation requires an assumption of either radial or PKN geometry. In most cases, we recommend the radial assumption. The PKN assumption can be used if there is strong evidence of height confinement in the layer. In many cases, the diameter calculated from the DFIT interpretation assuming radial geometry is less than or close to the 'height' that is under consideration for a PKN interpretation. In this case, the radial interpretation is the preferred choice.

To minimize uncertainty caused by unknown fracture geometry, it is preferable to perform DFIT's with relatively low injection volume (5-20 bbl). With larger injection volume, the fracture will be larger and more likely to hit stress barriers that limit height (or worse, low stress layers that capture the fracture). Because these stress contrasts complicate the interpretation and may be difficult to predict, lower injection volume reduces uncertainty. Also, with lower volume, the onset of impulse flow occurs sooner, improving the pore pressure estimate and increasing the probability that it will be possible to derive an impulse-flow permeability estimate.

Conversely, Craig and Jackson (2017) recommend pumping DFIT's with more than 100 bbl. They argue that a large fracture is needed to sample a sufficiently large volume of rock. To address concerns regarding heterogeneity, we recommend performing multiple DFIT's in different wells in the same interval and checking for consistency. In the field dataset reviewed in this study, the tests were generally performed with 5-40 bbl of injection, and we observed good consistency in permeability estimates between neighboring wells. This result supports the position that fractures created by 5-40 bbl of injection are large enough to sample a representative volume of rock.

In Section A.10.i, we derive equations that can be used to estimate leakoff coefficient from dP/dG. Commonly, the G-function leakoff calculation is performed using the equations derived by Valko and Economides (1999). However, these equations neglect the impact of wellbore storage, which is

nonnegligible in most DFIT's. The calculation requires estimation of the fracture size and requires an estimate of Shmin. Commonly, equations provided by Valko and Economides (1999) are used to estimate fracture size. However, these equations are only valid in the case of zero leakoff and zero wellbore storage. If wellbore storage coefficient and leakoff coefficient are set to zero in the equations in Section A.10.i, they simplify to the relations from Valko and Economides (1999).

In the analysis of the Utica DFIT, a PKN geometry is assumed with height of 110 ft. If the analysis is repeated with a radial assumption, the diameter is estimated to be 180 ft, and the permeability estimates are about 30% lower.

When applied to the Utica dataset, the G-function estimate for leakoff coefficient is 9.2e-5 ft/min^(1/2). The leakoff coefficient can be converted to permeability from the definition of leakoff coefficient for 'reservoir dominated flow' (Equation 19). This assumes that the impact of the filtrate zone is zero. The conversion to permeability uses the viscosity and compressibility of the mobile fluid phase in the reservoir, not the viscosity and compressibility of the injection fluid. We implicitly neglect any other potential multiphase flow effects, such as capillary pressure, and neglect the possibility of pressure dependent permeability. Below, we discuss comparison of impulse linear permeability estimates with G-function permeability estimates to assess the impact of these additional processes. The G-function permeability estimate is 27 nd.

Next, permeability can be estimated from the h-function method (Section A.10.ii). The h-function integrates the effective pressure response using a time-convolution integral of the Carter leakoff solution, accounting for the change in pressure over time. Fracture surface area is estimated using a mass balance equation accounting for wellbore storage and fluid leakoff.

The h-function method is related to the method of Mayerhofer et al. (1995). One difference is that Mayerhofer et al. (1995) use a convolution integral of the constant rate solution, and then estimate leakoff rate, whereas the h-function directly integrates the constant pressure solution. The method of Mayerhofer et al. (1995) requires an estimate of fracture area. As with the G-function method, the equations from Valko and Economides (1999) are sometimes used to estimate area with the method of Mayerhofer et al. (1995). But as described above, this technique neglects wellbore storage and leakoff. The h-function method is also related to the technique described by Wang and Sharma (2018).

Sometimes, fracture size is estimated with the Mayerhofer method by using an equation for predicting the time to impulse linear flow (Equation 3 from Craig et al., 2002). This equation is borrowed from conventional well test analysis. While it is valid in the context for which it was originally developed (Section 6.10.1 from Lee and Wattenbarger, 1996), the physics of a DFIT are very different, and there is not a theoretical justification for applying it to predict the timing of impulse linear flow in a DFIT. Simulation results indicate that it is often inaccurate. It not even directionally accurate in predicting the onset of impulse linear flow. For example, increasing Young's modulus causes a larger fracture, more surface area, earlier fracture contact, and earlier impulse linear flow (because contact accelerates the onset of impulse linear, as discussed by McClure, 2017). Yet, the relation from Craig et al. (2002) predicts that with more fracture surface area, impulse linear flow will happen later.

If the method of Mayerhofer et al. (1999) is applied with an accurate estimate of fracture size, then it is expected to yield an accurate estimation of permeability.

When applied to the transient in Figure 1, the h-function permeability estimate is 14 nd. Similar to the G-function permeability estimate above, this estimate neglects any potential multiphase flow effects.

Impulse linear is not present in Figure 1. However, if it were present, permeability could be estimated from dP/d(t^(-1/2)), using the standard impulse flow solutions (Section A.10.iii). As with the other linear methods, surface area can be estimated from a mass balance relation (Section A.10.iii). Unlike the G-function and h-function methods, the impulse linear permeability estimate is unaffected by multiphase leakoff effects or the potential for pressure dependent permeability. It is controlled by the pressure transient

in the reservoir away from the filtrate zone. Therefore, this estimate, if available, may be considered more representative of reservoir flow behavior and more applicable to reservoir engineering calculations of production.

In our field dataset, impulse linear was present in a substantial percentage of tests. In these tests, we observed that the impulse linear permeability estimate was usually 2-5 times smaller than the G-function and h-function estimates. Because of this observation, in cases when an impulse linear estimate is not available, it may be advisable to reduce the permeability estimate from the G-function or h-function methods by 3-fold when used in rate-transient or reservoir engineering calculations.

Barree et al. (2015a) propose that permeability can be related to the time to closure (as estimated from the tangent method), without considering the effect of injection volume, fluid viscosity, Young's modulus, fluid compressibility, or any other parameters. Simulations and comparison with field data indicate that this method is often severely inaccurate. We performed sensitivity analysis simulations in which we held permeability constant, but varied parameters such as viscosity (difference between gas and oil), modulus, and injection volume. The time to 'closure' (as picked by the tangent method) varied widely, resulting in greatly different permeability estimates from the method of Barree et al. (2015a), even though the permeability was the same in all simulations.

In the Utica DFIT, using the tangent method of picking closure, the time to closure is 1960 min. The injection duration is 9.7 min. Therefore, the equation proposed by Barree et al. (2015a) implies that permeability is equal to 1.6 microdarcy. This estimate is almost 100 times too high.

3.1.8 Permeability estimation from radial flow

As discussed in Section 3.1.5, we believe that the late-time transient in Figure 5 is false radial caused by interaction of evolving fracture stiffness after contact with multiphase flow effects. However, for comparison, we can use it to estimate permeability. The permeability-height product (kh) is estimated using the impulse radial solution (Section A.10.iv). Permeability is estimated by dividing kh by the estimate for height. If PKN geometry is assumed, then height is known. If radial geometry is assumed, we use the mass balance approach to estimate diameter, and set height equal to diameter.

The radial permeability estimate from the example dataset is 734 nd. This estimate is roughly 50x greater than the estimates from the G-function and h-function methods. The overestimate is consistent with expectation from simulation results and comparison with field data, as discussed in Section 3.1.5.

In this case, the operator had already evaluated, and discarded, the radial permeability estimate. The operator's diagnostics and analysis (performed prior to this DFIT study) suggested that the permeability is in the range of 10-20 nd, similar to the values calculated in Section 3.1.7 (Cipolla et al., 2018).

We observed a false radial signature in the majority of field DFIT's that we reviewed from a gas reservoir, involving tests in the Montney, Marcellus, and Utica. False radial was also observed in every DFIT simulation we performed of a gas reservoir. In these cases, using the false radial yielded a large overestimate of permeability.

3.1.9 Estimating average aperture versus effective stress

Using the technique in Section A.14, it is possible to derive an approximate plot of average aperture versus effective stress. Figure 7 shows the inferred relationship for the Utica DFIT.

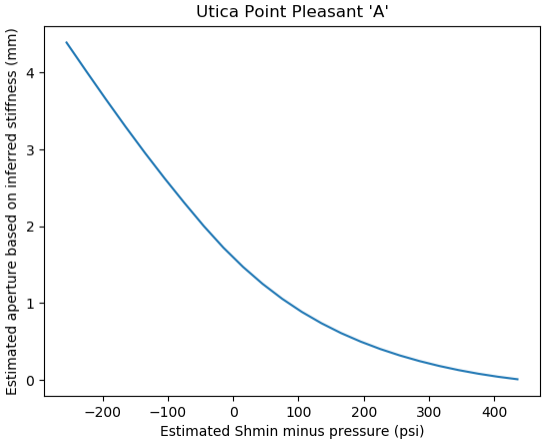

Figure 7: Approximate average aperture versus Shmin minus pressure for the Utica DFIT.

Figure 7 indicates that the contact pressure (when the system begins to stiffen) occurs when inferred aperture is around 2 mm. This is typical of the field data reviewed in this study: the aperture at the contact pressure was usually inferred to be in the range of 0.5 – 3 mm.

It is an important finding that the system begins to stiffen at an aperture on the order of millimeters. This finding is consistent with the finding from Branagan et al. (1996) that the residual tilt at late-time was 20% of the maximum observed tilt, experimental results from (Suarez-Rivera et al., 2013) showing macroscopic complexity in hydraulic fracture geometry, and DFIT analyses from Wang and Sharma (2018).

McClure et al. (2016) defined 'fracture closure' as being equivalent to what we are now calling the 'contact pressure' – the pressure at which the walls begin to contact and the system stiffens. The problem with the definition from McClure et al. (2016) is that it may seem counterintuitive to define 'closure' as occurring at a point when the average fracture aperture is still substantial.

3.2 Comparison with simulation

A numerical simulation was performed based on the parameters inferred from the data (Figure 8). The simulation is performed with permeability of 14 nd, Shmin equal to 7975 psi, pore pressure equal to 6900 psi, and near-wellbore pressure drop coefficient of 1500 psi/bpm^(1/2). The simulations appear very similar to the actual data (Figure 1 and Figure 5). The log-log plot indicates a bend into a -1 slope after the hump in t*dP/dt. The simulation shows a -1/2 slope after the -1 slope. This is not visible in the data, but the actual test terminated prior to 10^4 minutes, and the -1/2 slope in the simulation does not develop until after 10^4 minutes.

In order to improve the match to data, it was necessary to vary the W_0 and $\sigma_{n,ref}$ parameters from the Willis-Richards et al. (1995) equation for fracture aperture after contact (Equation 1). This was necessary because the shape of the aperture versus effective stress curve has a significant effect on the shape of the transient in the period after contact and prior to impulse flow. Permeability, pore pressure, and Shmin were not varied to match the data – the parameters were taken directly from the interpretation performed prior to running the simulation.

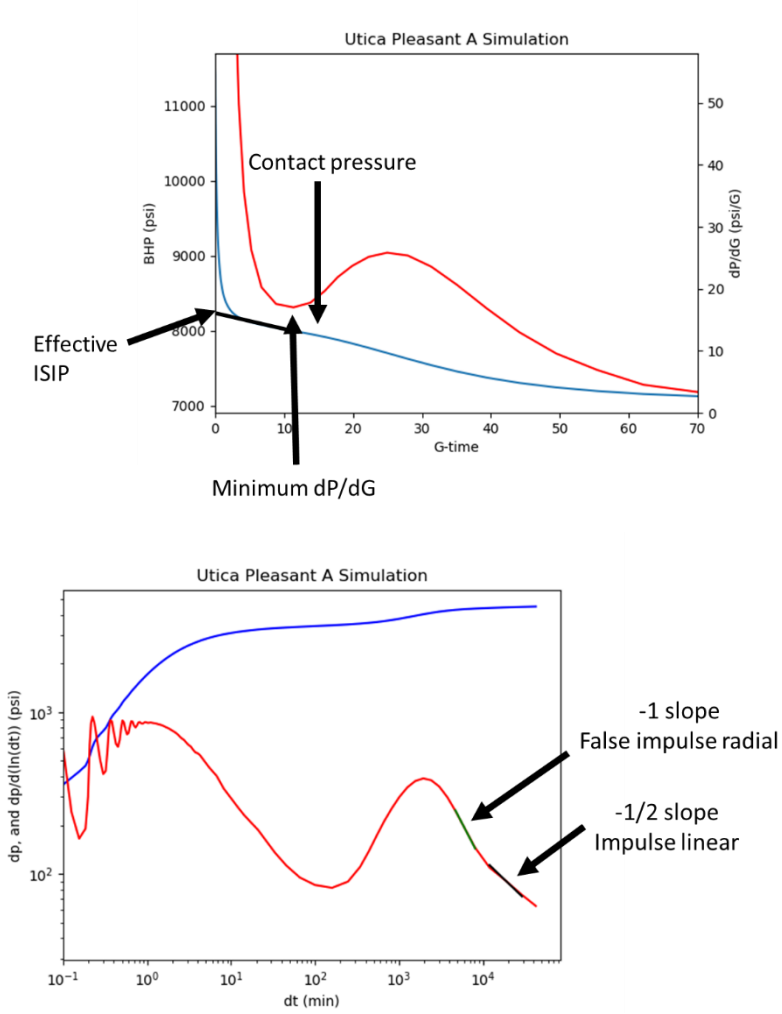

Figure 8: DFIT simulation based on the Utica DFIT.

3.3 Other field examples

Figure 9 shows results from a DFIT performed in an oil well in the Wolfcamp shale (WHP is plotted without adjustment to BHP). Approximately 3000 psi of near-wellbore pressure drop dissipates in the first 30 minutes after shut-in. The dP/dG plot shows good indication of contact, and the log-log plot shows a -1/2 slope after the hump in t*dP/dt. Using a radial fracture geometry, the G-function method yields a permeability estimate of 289 nd; the h-function method yields an estimate of 401 nd, and the impulse linear trend yields an estimate of 162 nd.

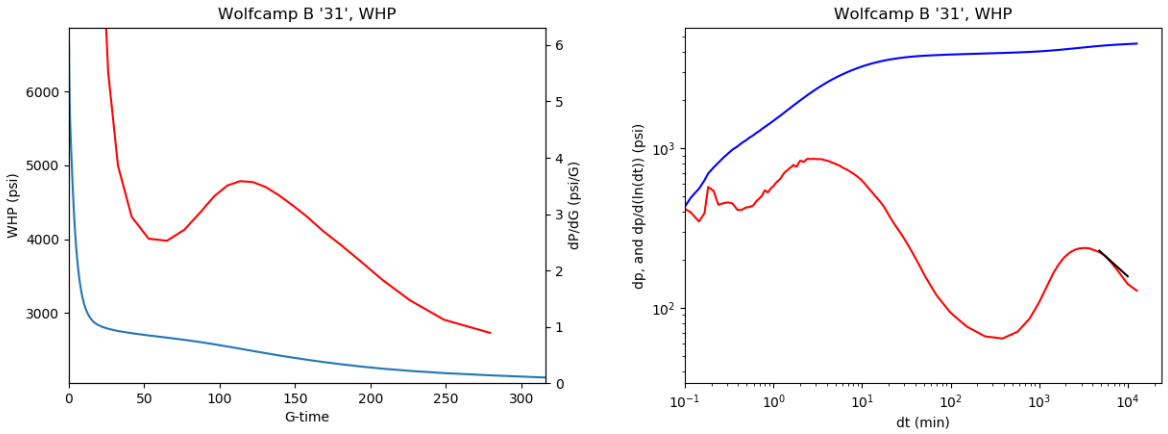

Figure 9: G-function and log-log plots for a DFIT performed in the Wolfcamp B. The G-function plot shows measured WHP.

DFIT's were performed in all five wells in this pad. All five were landed in the Wolfcamp B. They all show thousands of psi of near-wellbore pressure drop and have good indication of contact, as indicated from dP/dG increasing from a minimum. The estimates of Shmin are all within 150 psi of each other. The G-function permeability estimates are: 168 nd, 212 nd, 289 nd, 188 nd, and 638 nd. The h-function permeability estimates are: 204 nd, 137 nd, 401 nd, 142 nd, and 619 nd. Three of the DFIT's show an indication of impulse linear. The impulse linear permeability estimates are 64 nd, 162 nd, and 44 nd. None of the DFIT's shown an indication of impulse radial.

Figure 10 shows a dP/dG plot from a field DFIT in a vertical well the Lower Eagle Ford. As expected from a vertical well (in a non-thrust faulting regime), the near-wellbore tortuosity pressure drop is minimal. The estimate for Shmin is 12,076 psi. Assuming radial geometry, the G-function method permeability estimates is 171 nd, and the h-function method estimate is 126 nd.

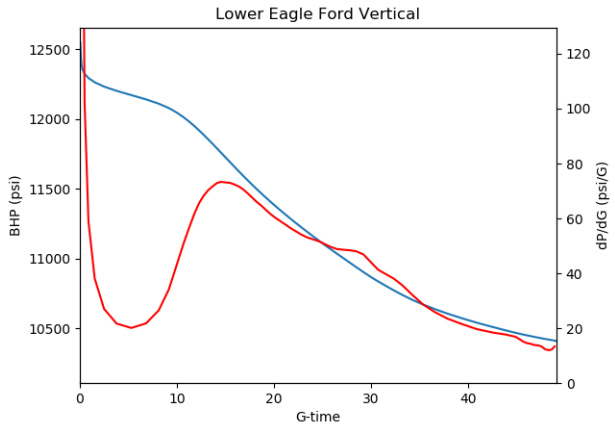

Figure 10: dP/dG and pressure versus G-time for a DFIT in a vertical well in the Lower Eagle Ford.

4. Discussion

4.1 Tests without a clear pick for contact pressure

The clarity of the pick for contact pressure can be assessed from the separation between the minimum and maximum dP/dG. If there is not good separation, a clear pick may also be possible if an inflection can be identified from the relative stiffness plot. Nevertheless, in some tests, a clear pick is not possible. Figure 11 shows an example of a test with monotonically decreasing dP/dG and a smoothly, gradually increasing relative stiffness.

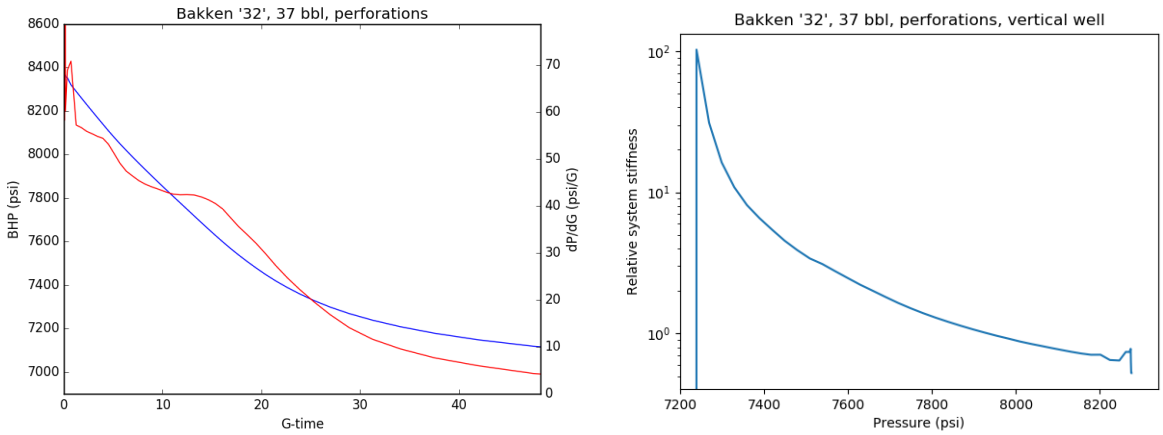

Figure 11: G-function plot and relative stiffness plot for a DFIT performed in the Middle Bakken (in Figure 11a, blue is pressure and red is dP/dG). It is not possible to identify the contact pressure or estimate Shmin.

By performing simulations under a variety of conditions, we identified processes that can cause monotonically decreasing dP/dG:

1. If a significant volume of fluid has been pumped into the formation prior to the DFIT, such that the DFIT involves reinjection into a pre-existing, previously-created hydraulic fracture.
2. If injection occurs directly into a highly conductive natural fracture.
3. If the hydraulic fracture intersects a highly conductive natural or pre-existing hydraulic fracture.
4. If the matrix permeability divided by formation fluid viscosity is sufficiently high (>0.01-0.1 md/cp).
5. If near-wellbore pressure drop is very severe, masking the pressure transient in the far-field fracture.

For the first four scenarios listed above, dP/dG is monotonic because the fracture walls contact almost instantly after shut-in (or perhaps, never fully separated). If injection reopens a pre-existing hydraulic or natural fracture, there is not any ‘toughness’ that must be overcome in order to propagate the effective ‘tip’ of reopening. As a result, the fracture opens just enough to conduct flow. After shut-in, the walls contact very rapidly, and fluid continues to flow outward into the rest of the pre-existing fracture. In scenario #3, the fracture walls contact rapidly because fluid flows out into the pre-existing fracture. In scenario #4, the fracture walls contact rapidly because growth is limited by leakoff, rather than resistance to propagation at the tip. In scenario #5, the pinch-point caused by near-wellbore pressure drop is so severe that the real pressure transient in the hydraulic fracture is not observed.

If the test in Figure 11 was in a vertical well, it might be justifiable to assume that there is not any near-wellbore tortuosity, and the ISIP could be taken as an estimate for Shmin (because of the 'rapid contact’ interpretations #1-#4). But because this test is in a horizontal well, it is unclear whether to interpret that the fracture walls have rapidly contacted or to interpret that near-wellbore pressure drop is obscuring the true transient (or a combination of both). Because of these uncertainties, a test in a horizontal well without clear evidence of a contact pressure cannot be confidently interpreted. In either vertical or horizontal wells, it will be impossible to estimate fracture area and permeability because the net pressure cannot be estimated. It might be possible to estimate permeability from impulse radial flow. If impulse linear or radial flow is reached, it will be possible to estimate pore pressure.

4.2 Impact of the permeability estimate

Rate-transient analysis (RTA) of production data in shale typically indicates linear flow. By matching the linear flow equation to the production data, it is possible to derive an estimate for $A\sqrt{k}$. However, without

an independent estimate for permeability, the RTA match is nonunique. With a DFIT permeability estimate, it is possible to uniquely estimate effective fracture area from the $A\sqrt{k}$ value taken from the RTA.

In the Utica dataset, the false/invalid radial flow evaluation and the method from Barree et al. (2015a) yield a 50-100-fold overestimate of permeability. Holding $A\sqrt{k}$ constant, this implies that the effective fracture area (or if height is assumed, effective fracture length) will be underestimated by a factor of 7-10.

The analysis provided by Barree et al. (2015b) may be an example of the consequences of overestimated permeability in a gas reservoir. They analyze a gas shale well with DFIT-derived permeability and an RTA match to production data. They estimate the effective fracture length to be just 35 ft. This estimate seems implausibly low.

To test the impact on net-present value, we history matched ResFrac simulations to the Utica well production data, using either 1 microdarcy or 20 nd as the permeability estimate. Then, we performed a series of simulations with different cluster and well spacing and performed simple economic calculations of net-present value. The high and low permeability models yielded different optimal designs. Applying the optimal design from the 'high permeability' model to the 'low permeability' model resulted in large reduction in net present value. The details of this comparison will be shown in a separate, standalone paper. The analysis shows that improved accuracy from the DFIT permeability estimate can improve fracture design and well placement and significantly increase return on investment.

5. Conclusions

By integrating detailed numerical simulations, field data, operator experience, and mathematical analysis, we developed a step-by-step procedure for estimating stress, permeability, and pore pressure from DFIT's in low permeability formations.

- Near-wellbore pressure drop typically causes 1000s of psi of pressure drop at early time in DFIT's in horizontal wells. If this occurs, then for tens of minutes after shut-in, pressure measured in the well is much higher than the pressure in the far-field hydraulic fracture. The effective ISIP (an estimate for the pressure in the fracture at shut-in) can be estimated from a G-function plot.
- Analogous to the g-function, the h-function is proportional to the cumulative volume of fluid leaked off from the fracture since the start of injection. Unlike the g-function, the h-function accounts for deviation from Carter leakoff as the pressure in the fracture decreases. The h-function is useful in mathematical derivations used for permeability estimation and for the construction of a relative stiffness plot.
- The G-function and h-function methods can be used to estimate permeability from the data prior to impulse flow. We derive mass balance equations for jointly inferring permeability and fracture size. Unlike equations commonly used in the literature (Valko and Economides, 1999), these equations consider wellbore storage and leakoff.
- Impulse linear flow can be used to estimate permeability as long as fracture area can be estimated. Similar to the G-function and h-function methods, permeability can be jointly estimated with area using a mass balance equation.
- Simulations show that a variety of processes can cause the appearance of impulse radial, even in situations where flow is not actually radial. This problem is especially severe in gas shale, where false radial is common in both simulation results and in real data. Analysis based on false radial flow typically leads to a 10-100x overestimate of permeability. Genuine radial is most likely to occur in low volume DFIT's and in formations with permeability divided by viscosity greater than 1 microdarcy/cp.
- The G-function and h-function permeability estimates are usually similar. The G-function method is more sensitive to error due to elevated dP/dG from near-wellbore pressure drop. With field data, impulse linear permeability estimates are usually 2-5 times lower than the G-function and h-function methods. The G-function and h-function estimates may be impacted by multiphase effects or by

pressure dependent permeability. Therefore, the impulse linear flow permeability estimate is typically preferred for reservoir engineering calculations. If impulse linear flow is not available, the G-function or h-function methods may be adjusted downward by about 3-fold. There is moderate uncertainty in the permeability estimates, and modelers should have reasonable freedom to modify permeability if needed to match production data.

- The magnitude of the minimum principal stress can be estimated by identifying the 'contact pressure' which is the pressure at which the fracture walls come into contact and the system begins to stiffen. The minimum principal stress can be estimated to be approximately 75 psi below the contact pressure. This is effectively the 'compliance method' of picking 'fracture closure' (McClure et al., 2016). However, we have defined the new term 'contact pressure' to avoid confusion with a variety of other definitions of 'closure.' Rather than using a plot of G*dP/dG (as recommended by McClure et al., 2016), we recommend identifying the contact pressure from a plot of dP/dG or from a relative stiffness plot.
- It is possible to approximately infer the relationship between aperture and effective stress. Field data shows that the average fracture aperture is between 0.5-3 mm at the contact pressure, and continues to be substantial when the fluid pressure is equal to the minimum principal stress. This is evidently the manifestation of the roughness of in-situ hydraulic fractures.
- DFIT permeability estimates have direct implication for fracture design and can significantly impact economic returns.

Acknowledgements

We gratefully acknowledge the financial support of ConocoPhillips Company, Hess Corporation, Shell International Exploration and Production Inc., Equinor, Keane Group, Range Resources Corporation, and Apache Corporation. We also want to recognize the important contributions of the study participants who are not listed as coauthors.

References

Ayoub, J. A., D. P. Bourdet, Y. L. Chauvel. 1988. Impulse testing. SPE Formation Evaluation **3** (3): 534-546, doi: 10.2118/15911-PA.

Barree, R. D., H. Mukherjee. 1996. Determination of pressure dependent leakoff and its effect on fracture geometry. SPE 36424. Paper presented at the 71st Annual Technical Conference and Exhibition, Denver, CO.

Barree, R. D., V. L. Barree, and D. P. Craig. 2009. Holistic fracture diagnostics: Consistent interpretation of prefrac injection tests using multiple analysis methods. SPE 107877. Paper presented at the SPE Rocky Mountain Oil & Gas Technology Symposium, Denver, CO.

Barree, R. D., J. L. Miskimins, and J. V. Gilbert. 2015a. Diagnostic fracture injection tests: common mistakes, misfires, and misdiagnoses. SPE Production & Operations **30** (2): 84-98, doi: 10.2118/169539-PA.

Barree, R. D., S. A. Cox, J. L. Miskimins, J. V. Gilbert, and M. W. Conway. 2015b. Economic optimization of horizontal-well completions in unconventional reservoirs. SPE Production & Operations **3** (4): 293-311, doi: 10.2118/168612-PA.

Barree, R. D. and J. L. Miskimins. 2016. Physical explanations of non-linear derivatives in diagnostic fracture injection test analysis. SPE 179134-MS. Paper presented at the SPE Hydraulic Fracturing Technology Conference, The Woodlands, TX.

Barton, N., S. Bandis, K. Bakhtar. 1985. Strength, deformation and conductivity coupling of rock joints. *International Journal of Rock Mechanics and Mining Sciences & Geomechanics Abstracts* **22** (3): 121-140, doi: 10.1016/0148-9062(85)93227-9.

Bazan, Lucas W. and Bruce R. Meyer. 2015. Fracture complexity: analysis methodology and signature pressure behavior of hydraulic fracture propagation from horizontal wellbores. SPE 176919. Paper presented at the SPE Asia Pacific Unconventional Resources Conference and Exhibition, Brisbane, Australia.

Bird, R. Byron, Warren E. Stewart, Edwin N. Lightfoot. 2006. Transport Phenomena, 2nd edition, John Wiley & Sons, Inc.

Blanton, T. L. and J. E. Olson. 1999. Stress magnitudes from logs: Effects of Tectonic Strains and Temperature. SPE Reservoir Evaluation and Engineering **2** (1), 62-68, doi: 10.2118/54653-PA.

Bourdet, D., T. M. Whittle, and A. A. Douglas. 1983. A new set of type curves simplifies well test analysis. World Oil: 95-106.

Branagan, P. T., N. R. Warpinski, B. Enger, and R. Wilmer. 1996. Measuring the hydraulic fracture-induced deformation of reservoirs and adjacent rocks employing a deeply buried inclinometer array: GRI/DOE multi-site project. SPE 36451. Paper presented at the SPE Annual Technical Conference and Exhibition, Denver, CO.

Carslaw, H. S., and J. C. Jaeger. 1959. Conduction of Heat in Solids. 2nd ed. Oxford University Press, Great Britain.

Castillo, J. L. 1987. Modified fracture pressure decline analysis including pressure-dependent leakoff. SPE 16417. Paper presented at the SPE/DOE Low Permeability Reservoir Symposium, Denver, CO.

Cipolla, Craig, Constance Gilbert, Aviral Sharma, and John LeBas. 2018. Case history of completion optimization in the Utica. SPE 189838-MS. Paper presented at the SPE Hydraulic Fracturing Technology Conference and Exhibition, The Woodlands, TX.

Clark, J. B. 1949. A hydraulic process for increasing the productivity of wells. Journal of Petroleum Technology **1** (1): 1-8.

Craig, David P., Ted D. Brown. 1999. Estimating pore pressure and permeability in massively stacked lenticular reservoirs using diagnostic fracture-injection tests. SPE 56600. Paper presented at the SPE Annual Technical Conference and Exhibition, Houston, TX.

Craig, David P., Mike J. Eberhard, Chad E. Odegard, and Muthukumarappan Ramurthy. 2002. Permeability, pore pressure, and leakoff-type distributions in Rocky Mountain Basins. SPE 75717. Paper presented at the SPE Gas Technology Symposium, Calgary, Alberta, Canada.

Craig, David P. 2014. New type curve analysis removes limitations of conventional after-closure analysis of DFIT data. SPE 168988-MS. Paper presented at the SPE Unconventional Resources Conference, The Woodlands, TX.

Craig, D. P. and T. A. Blasingame. 2006. Application of a new fracture-injection/falloff model accounting for propagating, dilated, and closing hydraulic fractures. SPE 100578. Paper presented at the SPE Gas Technology Symposium, Calgary, Alberta.

Craig, D. P., R. D. Barree, N. R. Warpinski, and T. A. Blasingame. 2017. Fracture closure stress: Reexamining field and laboratory experiments of fracture closure using modern interpretation methodologies. SPE 187038. Paper presented at the SPE Annual Technical Conference and Exhibition, San Antonio, TX.

Craig, David and Robert Jackson. 2017. Calculating the volume of reservoir investigated during a fracture-injection/falloff test DFIT. SPE 184820. Paper presented at the SPE Hydraulic Fracturing Technology Conference and Exhibition, The Woodlands, TX.

Cramer, D. D. and D. H. Nguyen. 2013. Diagnostic fracture injection testing tactics in unconventional reservoirs. SPE 163863. Paper presented at the SPE Hydraulic Fracturing Technology Conference, Woodlands, TX.

Cramer, D., Friehauf, K., Roberts, G., Whittaker, J. 2019. Integrating DAS, Treatment Pressure Analysis and Video-based Perforation Imaging to Evaluate Limited Entry Treatment Effectiveness. SPE 194334. Paper presented at the SPE Hydraulic Fracturing Technology Conference, Woodlands, TX.

Crouch, S. L. and A. M. Starfield. 1983. Boundary Element Methods in Solid Mechanics. George Allen & Unwin (Publishers), Ltd.

Delaney, Paul T., David D. Pollard, Joseph I. Ziony, and Edwin H. McKee. 1986. Field relations between dikes and joints: emplacement processes and paleostress analysis. Journal of Geophysical Research, **91** (B5): 4920-4938, doi: 10.1029/JB091iB05p04920.

Eaton, Ben A. 1969. Fracture gradient prediction and its application in oilfield operations. Journal of Petroleum Technology **21** (10): 1353-1360, doi: 10.2118/2163-PA

Economides, Michael J. and Kenneth G. Nolte, eds. 2000. Reservoir Stimulation. Wiley.

Economides, Michael and Tony Martin. 2008. Modern Fracturing – Enhancing Natural Gas Production. Energy Tribune Publishing.

Ehlig-Economides, Christine A. and Michael J. Economides. 2000. Chapter 2: Formation characterization: Well and reservoir testing. *In* Reservoir Stimulation, eds, Michael J. Economides and Kenneth G. Nolte, Wiley.

Gale, Julia F. W., Sara J. Elliott, and Stephen E. Laubach. 2018. Hydraulic fractures in core from stimulated reservoirs: core fracture description of HFTS slant core, Midland Basin, West Texas. Paper presented at the Unconventional Resources Technology Conference, Houston, TX.

Godbey, J. K., H. D. Hodges. 1958. Pressure measurements during formation fracturing operations. Petroleum Transactions, AIME 213: 65-69

Gringarten, Alain C., Henry J. Ramey, R. Raghavan. 1974. Unsteady-state pressure distributions created by a well with a single infinite conductivity vertical fracture. SPE Journal **14** (4): 347-360, doi: 10.2118/4051-PA.

Gu, H., J. L. Elbel, K. G. Nolte, A. H. D. Cheng, Y. Abousleiman. 1993. Formation permeability determination using impulse-fracture injection. SPE 25425. Paper presented at the Production Operations Symposium, Oklahoma City, OK.

Gulrajani, Sunil N. and K. G. Nolte. 2000. Chapter 9: Fracture Evaluation using Pressure Diagnostics. *In* Reservoir Stimulation, eds, Michael J. Economides and Kenneth G. Nolte, Wiley.

Haimson, Bezalel, Charles Fairhurst. 1967. Initiation and extension of hydraulic fractures in rocks. Society of Petroleum Engineers Journal **7** (3), doi: 10.2118/1710-PA.

Hawkes, R. V., R. Bachman, K. Nicholson, D. D. Cramer, and S. T. Chipperfield. 2018. Good tests cost money, bad tests cost more – a critical review of DFIT analysis gone wrong. SPE 191458. Paper presented at the SPE International Hydraulic Fracturing Technology Conference and Exhibition, Muscat, Oman.

Hickman, Stephen H., Mark D. Zoback. 1983. The interpretation of hydraulic fracturing pressure-time data for in-situ stress determination. In Hydraulic Fracturing Measurements, ed. M. D. Zoback and B. C. Haimson, 44-54. Washington D.C., National Academy Press.

Horne, Roland N. 1995. Modern Well Test Analysis: A Computer-Aided Approach, 2nd edition. Palo Alto, CA, Petroway, Inc.

Houze, Olivier P., Roland N. Horne, Henry J. Ramey. 1988. Pressure-transient response of an infinite conductivity vertical fracture in a reservoir with double-porosity behavior. SPE Formation Evaluation **3** (3): 510-518, doi: 10.2118/12778-PA.

Howard, George C. and C. R. Fast. 1957. Optimum fluid characteristics for fracture extension. Paper presented at the Spring Meeting of the Mid-Continental District, Division of Production, Tulsa, OK.

Hubbert, M. K., D. G. Willis. 1957. Mechanics of hydraulic fracturing. Journal of Petroleum Technology **9** (6): 153-168.

Jung, H., M. M. Sharma, D. D. Cramer, S. Oakes, and M. W. McClure. 2016. Re-examining interpretations of non-ideal behavior during diagnostic fracture injection tests. Journal of Petroleum Science and Engineering **145**: 114-136, doi: 10.1016/j.petrol.2016.03.016.

Kamal, Medhat M., ed. 2009. Transient Well Testing, Vol. Monograph Series Vol. 23, Society of Petroleum Engineers.

Kehle, Ralph O. 1964. The determination of tectonic stresses through analysis of hydraulic well fracturing. Journal of Geophysical Research **69** (2): 259-273, doi: 10.1029/JZ069i002p00259.

Lee, J. and R. Wattenbarger. 1996. Gas Reservoir Engineering. Society of Petroleum Engineers.

Liu, Guoqing, Christine Ehlig-Economides, and Jianlei Sun. 2016. Comprehensive Global Fracture Calibration Model. SPE 181856. Paper presented at the SPE Asia Pacific Hydraulic Fracturing Conference, Beijing, China.

Marongiu-Porcu, Matteo, Christine A. Ehlig-Economides, and Michael John Economides. 2011. Global model for fracture falloff analysis. SPE 144028. Paper presented at the SPE North American Unconventional Gas Conference and Exhibition, The Woodlands, TX.

Marongiu-Porcu, Matteo, Albertus Retnanto, Michael J. Economides, Christine Ehlig-Economides. 2014. Comprehensive fracture calibration test design. SPE 168634. Paper presented at the SPE Hydraulic Fracturing Technology Conference, The Woodlands, TX.

Mayerhofer, M. J. and M. J. Economides. 1993. Permeability estimation from fracture calibration treatments. SPE 26039. Paper presented at the SPE Western Regional Meeting, Anchorage, AK.

Mayerhofer, M. J., C. A. Ehlig-Economides, and M. J. Economides. 1995. Pressure-transient analysis of fracture-calibration tests. SPE 26527. Journal of Petroleum Technology **47** (3): 231-236.

McLennan, J. D., J.-C. Roegiers. 1982. How instantaneous are instantaneous shut-in pressures? SPE 11064. Paper presented at the 57th Annual Fall Technical Conference and Exhibition of the Society of Petroleum Engineers of AIME, New Orleans, LA.

McClure, M. W. 2012. Modeling and characterization of hydraulic stimulation and induced seismicity in geothermal and shale gas reservoirs. PhD Thesis, Stanford University, Stanford, California.

McClure, Mark W., Christopher A. J. Blyton, Hojung Jung, and Mukul M. Sharma. 2014. The Effect of Changing Fracture Compliance on Pressure Transient Behavior During Diagnostic Fracture Injection Tests. SPE 170956. Paper presented at the SPE Annual Technical Conference and Exhibition, Amsterdam, The Netherlands.

McClure, Mark W., Hojung Jung, Dave D. Cramer, and Mukul M. Sharma. 2016. The fracture compliance method for picking closure pressure from diagnostic fracture injection tests. SPE Journal 21 (4): 1321-1339, doi: 10.2118/179725-PA.

McClure, Mark. 2017. The spurious deflection on log-log superposition-time derivative plots of diagnostic fracture-injection tests. SPE Reservoir Evaluation & Engineering 20 (4), doi: 10.2118/186098-PA.

McClure, Mark. 2019. Discussion of the Paper "SPE-187038-MS: Fracture Closure Stress: Reexamining Field and Laboratory Experiments of Fracture Closure Using Modern Interpretation Methodologies." arXiv:1904.07126

McClure, Mark and Charles Kang. 2018. ResFrac Technical Writeup. arXiv:1804.02092.

Meng, Chunfang, Lingli Wei, Roger Yuan. 2014. Coupled fluid flow and geomechanics modeling for DFIT analysis in unconventional gas development. Paper presented at the International Petroleum Technology Conference, Kuala Lumpur, Malaysia, doi: 10.2523/18159-MS.

Mukherjee, H. 1991. Extension of fracture pressure decline curve analysis to fissured formations. SPE 21872. Paper presented at the Rocky Mountain Regional Meeting and Low-Permeability Reservoir Symposium, Denver, CO.

Nolte, Kenneth. 1979. Determination of fracture parameters from fracturing pressure decline. SPE 8341. Paper presented at the Annual Fall Technical Conference and Exhibition of the Society of Petroleum Engineers, Las Vegas, NV.

Nolte, K. G., J. L. Maniere, and K. A. Owens. 1997. After-closure analysis of fracture calibration tests. SPE 38676. Paper presented at the 1997 Annual Technology Conference and Exhibition of the Society of Petroleum Engineers, San Antonio, TX.

Padmakar, A. S. 2013. Geomechanics coupled reservoir flow simulation for diagnostic fracture injection test design and interpretation in shale reservoirs. SPE 166201. Paper presented at the SPE Annual Technical Conference and Exhibition, New Orleans, LA.

Perkins, T. K., and J. A. Gonzalez. 1985. The effect of thermoelastic stresses on injection well fracturing **25**(1): 78-88, doi: 10.2118/11332-PA.

Raaen, A. M., E. Skomedal, H. Kjorholt, P. Markestad, D. Okland. 2001. Stress determination from hydraulic fracturing tests: the system stiffness approach. International Journal for Rock Mechanics and Mining Sciences **38** (4): 529-541, doi: 10.1016/S1365-1609(01)00020-X.

Scholz, Christopher H. 2010. A note on the scaling relations for opening mode fractures in rock. Journal of Structural Geology **32**, doi: 10.1016/j.jsg.2010.09.007.

Shou, Keh-Jian, Eduard Siebrits, Steven L. Crouch. 1997. A higher order displacement discontinuity method for three-dimensional elastostatic problems. International Journal of Rock Mechanics and Mining Sciences **34** (2): 317-322, doi: 10.1016/S0148-9062(96)00052-6.

Smith, Michael Berry and Carl T. Montgomery. 2015. Hydraulic Fracturing. CRC Press.

Sneddon, I. N. 1946. The distribution of stress in the neighborhood of a crack in an elastic solid. Proceedings of the Royal Society of London Series A **187** (1009): 229-260, doi: 10.1098/rspa.1946.0077

Soliman, M. Y. and Talal Gamadi. 2012. Testing tight gas and unconventional formations and determination of closure pressure. SPE 150948. Paper presented at the SPE/EAGE European Unconventional Resources Conference and Exhibition, Vienna, Austria.

Soliman, M. Y., C.S. Kabir. 2012. Testing unconventional formations. Journal of Petroleum Science and Technology **92-93**: 102-109, doi: 10.1016/j.petrol.2012.04.027.

Spivey, John P. and W. John Lee. 2013. Applied Well Test Interpretation. SPE Textbook Series, volume 13.

Stewart, George. 2011. Well Test Design and Analysis. PennWell Corp.

Suarez-Rivera, Roberto, Jeff Burghardt, Sergei Stanchits, Eric Edelman, and Aniket Surdi. 2013. The effect of rock fabric on fracture complexity for improving completion design and well performance. Paper presented at the International Petroleum Technology Conference, Beijing, China.

Theis, Charles V. 1935. The relationship between the lowering of the Piezometric surface and the rate and duration of discharge of a well using ground-water storage. Eos, Transactions, American Geophysical Union **16** (2): 519-524, doi: 10.1029/TR016i002p00519.

Valko, P. P. and M. J. Economides. 1999. Fluid-leakoff delineation in high-permeability fracturing. SPE Production & Facilities **14** (2), doi: 10.2118/56135-PA.

Vogler, D., R. R. Settgast, C. Annavarapu, C. Madonna, P. Bayer, and F. Amann. 2018. Experiments and simulations of fully hydro-mechanically coupled response of rough fracture exposed to high-pressure injection. Journal of Geophysical Research: Solid Earth **123**: 1186-1200, doi: 10.1002/2017JB015057.

Wallace, J., C. S. Kabir, C. L. Cipolla. 2014. Multiphysics investigation of diagnostic fracture injection tests in unconventional reservoirs. SPE 168620. Paper presented at the SPE Hydraulic Fracturing Technology Conference, The Woodlands, TX.

Wang, HanYi and Mukul M. Sharma. 2017. New variable compliance method for estimating in-situ stress and leak-off from DFIT data. SPE 187348. Paper presented at the SPE Annual Technical Conference and Exhibition, San Antonio, TX.

Wang, HanYi and Mukul M. Sharma. 2018. Estimating unpropped fracture conductivity and compliance from diagnostic fracture injection tests. SPE 189844. Paper presented at the SPE Hydraulic Fracturing Technology Conference & Exhibition, The Woodlands, TX.

Warpinski, Norman R. 1991. Hydraulic fracturing in tight, fissured media. Journal of Petroleum Technology, **43** (2), doi: 10.2118/20154-PA.

Weijers, L., L. G. Griffin, H. Sugiyama, T. Shimamoto, S. Takada, K. K. Chong, J. M. Terracina, and C. A. Wright. 2002. The first successful fracture treatment campaign conducted in Japan: Stimulation challenges in a deep, naturally fractured volcanic rock. SPE 77678. Paper presented at the Annual Technical Conference and Exhibition, San Antonio, TX.

Willis-Richards, J., K. Watanabe, H. Takahashi. 1996. Progress toward a stochastic rock mechanics model of engineered geothermal systems. *Journal of Geophysical Research* **101** (B8): 17481-17496, doi: 10.1029/96JB00882.

Witherspoon, P. A., J. S. Y. Wang, K. Iwai, J. E. Gale. 1980. Validity of cubic law for fluid flow in a deformable rock fracture. Water Resources Research **16** (6): 1016-1024, doi: 10.1029/WR016i006p01016.

Wright, Chris. 2000. Section 9E: Rate step-down test analysis – a diagnostic for fracture entry. *In* Reservoir Stimulation, eds, Michael J. Economides and Kenneth G. Nolte, Wiley.

Yew, Ching H. and Xiaowei Weng. 2015. Mechanics of Hydraulic Fracturing. Gulf Professional Publishing.

Zanganeh, Behnam, Christopher R. Clarkson, Jack R. Jones. 2019. Reinterpretation of flow patterns during DFITs based on dynamic fracture geometry, leakoff and afterflow. SPE 189840. Paper presented at the SPE Hydraulic Fracturing Technology Conference, The Woodlands, TX.

Zhang, Junjing, Anton Kamenov, D. Zhu, A.D. Hill. 2013. Laboratory measurement of hydraulic fracture conductivities in the Barnett Shale. SPE 163839. Paper presented at the SPE Hydraulic Fracturing Technology Conference, The Woodlands, TX.

Zoback, Mark. 2007. Reservoir Geomechanics. Cambridge University Press.

List of variables

A: fracture surface area; does not count both sides of the fracture – ie, defined so that a fracture with sides of length 1 ft has area of 1 ft^2 (ft^2; m^2)
c_{fl}: compressibility of the fluid in the fracture (psi^-1; MPa^-1)
C_f: fracture conductivity (md-ft; m^3)
C_{fD}: dimensionless fracture conductivity
C_L: leakoff coefficient (ft/min^0.5; m/s^0.5)
C_{nw}: near-wellbore pressure drop coefficient (psi/(bpm)^.5; MPa/(m^3/s)^.5)
C_t: total system storage coefficient (bbl/psi; m^3/MPa)
c_t: total formation compressibility (psi^-1; MPa^-1)
C_w: wellbore storage coefficient (bbl/psi; m^3/MPa)
E': Plane strain Young's modulus
F_L: linear flow time function (dimensionless)
G: G-function (dimensionless)
G_c: G-function at closure (dimensionless)
g: g-function (dimensionless)
g_0: g-function at shut-in (dimensionless)
H: H-function (psi-min^.5; MPa-s^.5)
h: h-function (psi-min^.5; MPa-s^.5); or formation height (ft; m)
h_f: fracture height (ft; m)
k: permeability (md; m^2)
L_f: fracture length (ft; m)
m: mass of fluid in the wellbore/fracture system (lbs; kg)
P: fluid pressure (psi; MPa)
P_0: effective fluid pressure at shut-in (estimate for effective ISIP) (psi; MPa)
P_{eff}: effective fluid pressure (estimate for fluid pressure in the fracture) (psi; MPa)
$P_{ISIP,eff}$: effective ISIP (psi; MPa)
P_{res}: reservoir fluid pressure (psi; MPa)
$P_{w,init}$: fluid pressure at the beginning of injection (psi; MPa)
Q: volumetric flow rate (bpm; m^3/s)
R_f: fracture radius (ft; m)
r_w: wellbore radius (ft; m)
s: skin factor (unitless)
$S_{f,c}$: stiffness of a closed crack (psi/ft; MPa/m)
$S_{f,o}$: stiffness of an open crack (psi/ft; MPa/m)
S_{rel}: relative stiffness (min^-.5; s^-.5)
S_t: total system stiffness (psi/bbl; MPa/m^3)
t: time (various units; s)
t_e: duration of injection (min; s)
V: volume of the wellbore/fracture system (bbl; m^3)
V_f: volume of fluid in the fracture (bbl; m^3)
V_{inj}: volume of fluid injected (bbl; m^3)
V_L: volume of fluid leaked off from the fracture since the start of injection (bbl; m^3)
V_{Ls}: volume of fluid leaked off from the fracture since shut-in (bbl; m^3)
V_{slug}: volume of fluid injected as part of a slug test (bbl; m^3)
W: fracture aperture (inches; m)
W_0: fracture aperture when the walls come into contact (inches; m)
$W_{0,max}$: numerical parameter; maximum allowed value of W_0 in an element (inches; m)
β: near-wellbore pressure drop exponent (unitless)
ΔP_{nw}: pressure drop due to near-wellbore pressure drop (psi; MPa)

Δt: shut-in duration (min; s)
Δt_{peak}: shut-in duration at the peak value of G*dP/dG (min; s)
$\Delta\sigma_{n,back}$: additional normal stress on the fracture due to opening (psi; MPa)
η: fracturing efficiency (dimensionless)
μ: fluid viscosity (cp; MPa-s)
σ_n: normal stress (psi; MPa)
$\sigma_{n,c}$: contact stress (psi; MPa)
$\sigma_{n,ref}$: effective normal stress at which the aperture has decreased 90% from W_0 (psi; MPa)
τ: integration variable for time (min; s)
ϕ: porosity (unitless)

A. Appendix

This appendix reviews the physics of a DFIT pressure transient and provides mathematical derivation of interpretation techniques. All equations are provided in consistent (SI) units.

A.1 Decomposing the pressure derivative

From the chain rule, the derivative of pressure with respect to time can be written as:

$$\frac{dP}{dt} = \frac{dP}{dm}\frac{dm}{dt}, \tag{2}$$

where P is pressure, m is mass of fluid in the wellbore/fracture system, and t is time. Starting from Equation 2, McClure et al. (2016) showed that for a slightly compressible fluid:

$$\frac{dP}{dt} = \frac{1}{C_t}\frac{dV}{dt}, \tag{3}$$

where $\frac{\mathrm{dV}}{\mathrm{dt}}$ is the leakoff rate and C_t is the system storage coefficient (the volume of fluid released from the system per increment of pressure). Equation 3 provides a framework for understanding DFIT pressure transients. Changes in slope are caused by changes in either system storage coefficient or leakoff.

Equation 2 assumes that a single value of pressure can be used for the entire fracture. This implicitly assumes that the fracture is effectively infinite conductivity and neglects perforation and near-wellbore pressure drop. The effect of finite fracture conductivity is discussed in Section A.5.

A.2 System storage and contact

McClure et al. (2016) showed that the system stiffness (and its reciprocal, system storage) can be written as:

$$S_t = \frac{1}{C_t} = \frac{1}{C_w + \frac{A}{S_f} + V_f c_{fl}}. \tag{4}$$

where C_w is the wellbore storage coefficient, A is the area of the fracture, S_f is the fracture stiffness (equal to the reciprocal of the derivative of average fracture aperture with respect to pressure), V_f is the volume of the fracture, and c_{fl} is the compressibility of the fluid in the fracture. Equation 4 is valid during injection, and after shut-in: before, during, and after contact. Raaen et al. (2001) performed a similar decomposition of system stiffness for application to pumpin/flowback tests.

The wellbore storage coefficient has two components – the compressibility of the fluid in the well and the compressibility of the wellbore volume itself. Wellbore storage coefficient can be estimated directly from the injection data. At the beginning of injection, prior to breakdown or fracture opening, a plot of pressure versus cumulative injection volume forms a straight line. The slope is equal to the wellbore storage coefficient.

In these derivations, volumes and areas are written in terms of the *full* fracture volume and area, not the volume and area of *one-wing* of the fracture. Authors sometimes define terms using *one-wing* of the fracture. We prefer not to follow this convention because fractures can propagate radially, with complex geometry, or asymmetrically, and so in the general case it is not always meaningful to refer to 'one-wing' of a fracture. Also, sometimes authors define 'area' by counting *both sides* of the fracture. This is not the convention used in this paper. We define area according to the convention that a square fracture with length and height of 1 ft has an area of 1 ft^2.

We define the 'contact pressure' as being the pressure at which the fracture walls come back into contact and the system begins to stiffen. Prior to contact, the fracture stiffness can be written from an analytical solution based on the geometry of the fracture and the mechanical properties of the rock. The two common geometry assumptions are radial and PKN. PKN fracture geometry applies to a fracture that has length much greater than height.

If the fracture is radial, the stiffness is (Table 2-2 from Ehlig-Economides and Economides, 2000):

$$S_{f,o}(radial) = \frac{3\pi E'}{16 R_f}, \tag{5}$$

where $S_{f,o}$ is the stiffness of an open crack, E' is the plane strain Young's modulus, and R_f is the radius. If the fracture has PKN geometry, the stiffness is written as:

$$S_{f,o}(PKN) = \frac{2E'}{\pi h_f}, \tag{6}$$

where h_f is the assumed fracture height. Once contact occurs, the fracture begins to stiffen because of contact stress created by the contacting fracture walls. The total stiffness can be written as (McClure et al., 2016):

$$S_f = S_{f,o} + S_{f,c}, \tag{7}$$

where $S_{f,c}$ is the additional stiffness due to contact. The contact stiffness is equal to:

$$S_{f,c} = \frac{1}{\frac{dW}{dP}}, \tag{8}$$

where W is the fracture aperture (calculated as a function of effective normal stress). Sometimes, authors differentiate between fracture void aperture and hydraulic aperture (McClure, 2012), but in this work, they are assumed to be equal.

Prior to contact, $S_{f,c}$ is equal to zero. After contact, the parameter $S_{f,c}$ begins to increase and asymptotically approaches infinity as effective normal stress approaches infinity. $S_{f,c}$ can be calculated from an empirical relation between aperture and effective normal stress.

The resulting relation for contact stiffness is:

$$S_{f,c} = \frac{\sigma_{n,ref}}{9W_0}\left(1 + \frac{9(\sigma_n - P)}{\sigma_{n,ref}}\right)^2. \tag{9}$$

Equation 9 indicates that $S_{f,c}$ is nonzero at the moment of contact, which implies a discontinuous jump in stiffness at the point of contact. It is unclear whether this is realistic. In future work, it would be worthwhile to explore alternatives to Equation 1 that allow a smooth increase from contact stiffness from zero as contact occurs.

Even after 'contact' has occurred across the entire fracture, the walls of the fracture are not literally touching everywhere along the fracture. Instead, asperities cause solid-to-solid contact across only a fraction of the fracture area. As effective stress increases, the percentage of area with solid-to-solid contact increases. This process is implicit to Equation 1. The equation to be used to capture average fracture aperture without performing detailed modeling at the scale of individual asperities. As an example of the alternative approach, Vogler et al. (2018) performed small-scale modeling that captures individual asperities.

Prior to contact, force balance requires that fracture effective normal stress is equal to zero (Crouch and Starfield, 1983). After contact, the effective normal stress becomes compressive and equal to the contact stress created by the contacting of the fracture walls. Contact stress can be calculated by solving for effective normal stress in a constitutive equation. Using Equation 1, contact stress is:

$$\sigma_n - P = \sigma_{n,c} = \frac{\sigma_{n,ref}}{9} \left(\frac{W_0}{W} - 1\right). \quad (10)$$

Because of fracture roughness, the fracture aperture is not zero at contact. This residual aperture creates a backstress so that the normal stress is slightly above Shmin when the walls come into contact. The backstress can be calculated as:

$$\Delta\sigma_{n,back} = WS_{f,o}. \quad (11)$$

The fluid pressure is equal to Shmin when the backstress is equal to the contact stress:

$$WS_{f,o} = \frac{\sigma_{n,ref}}{9} \left(\frac{W_0}{W} - 1\right). \quad (12)$$

There is a discrete change in the physics at the point when the walls come into contact – the contact stress begins to increase from zero. However, there is no meaningful change in the physics or discernable signal in the transient when pressure is equal to Shmin. Because there is not a signal in the data when pressure reaches Shmin, the difference between contact pressure and Shmin is a source of uncertainty when estimating Shmin.

Craig and Blasingame (2006) and Craig et al. (2017) define the total storage in a piece-wise fashion – neglecting different parts of the storage at different points during the test. In their definition, the $\frac{A}{S_f}$ term is negligible after 'closure,' implying that S_f is infinite. This assumption does not appear to be well-founded. With realistic values in Equation 4, the $\frac{A}{S_f}$ term is not negligible until pressure is hundreds or thousands of psi below Shmin.

A.3 G-function analysis

The G-function (also called G-time) is a monotonic transformation of Δt (shut-in time). Nolte (1979) derived the G-function (also called G-time) such that, under reasonable assumptions, the cumulative leakoff after shut-in is linearly proportional to G-time. A related function, the g-function, is derived to be linearly proportional to the cumulative leakoff from the start of injection (Castillo, 1987; Gulrajani and Nolte, 2000):

$$V_L(\Delta t) = 2AC_L\sqrt{t_e}\,g(\Delta t). \quad (13)$$

The G-function is defined as:

$$G(\Delta t) = \frac{4}{\pi}(g(\Delta t) - g(\Delta t = 0)). \quad (14)$$

The cumulative leakoff after shut-in is defined as:

$$V_{Ls}(\Delta t) = 2AC_L\sqrt{t_e}(g(\Delta t) - g(0)) = \frac{\pi}{2}AC_L\sqrt{t_e}G(\Delta t). \quad (15)$$

The exact form of the G and g functions depend on assumptions about fracture growth. However, there is little practical difference between the different forms of the g and G-functions. For example, within reasonable ranges, the cumulative leakoff at shut-in can be bounded with $g_0 = g(\Delta t = 0)$ is a number in the narrow range between 4/3 and $\frac{\pi}{2}$ (Equation 30 of the appendix from Gulrajani and Nolte, 2001). The most common form of the g-function is:

$$g(\Delta t) = \frac{4}{3}\left[\left(1 + \frac{\Delta t}{t_e}\right)^{1.5} - \left(\frac{\Delta t}{t_e}\right)^{1.5}\right]. \quad (16)$$

Because cumulative leakoff after shut-in is proportional to G-time, the derivative of cumulative leakoff with respect to G-time is equal to a constant. In the ideal case, fracture stiffness is constant prior to contact, and so the total system storage (and stiffness) are also constant prior to contact. Therefore, from Equation 3, a plot of pressure versus G-time should form a straight line (Castillo, 1987):

$$\frac{dP}{dG} = \frac{1}{C_t}\frac{dV}{dG} = constant. \quad (17)$$

If fracture geometry and mechanical properties of the rock are known, then Equation 17 can be solved for the leakoff coefficient (Nolte, 1979; Castillo, 1987; Gulrajani and Nolte, 2000).

If the fracture formed instantaneously during injection, then the G-function would be equivalent the square root of time. The square root scaling arises because the G-function assumes Carter leakoff. The G-function is not exactly equal to the square root of time because accounts for the progressive growth of the fracture during injection. As a result, the duration of leakoff is a function of position along the fracture area. Equation 24 from McClure (2017) provides a succinct derivation of the G-function for the special case that the fracture grows linearly with respect to time during injection.

A.4 Deviation from Carter leakoff

The G-function is derived based on the assumption of Carter leakoff (Nolte, 1979; Howard and Fast, 1957). For the simple case with no filtrate zone or filtercake, Carter leakoff can be derived as the solution the 1D diffusivity equation with a Dirichlet (constant pressure) boundary condition (Bird et al., 2007):

$$V_{Ls} = 4A\sqrt{\Delta t}(P - P_{res})\sqrt{\frac{\phi c_t k}{\pi \mu}} = 4AC_L\sqrt{\Delta t}. \quad (18)$$

The leakoff coefficient is defined from Equation 18 as:

$$C_L = (P - P_{res})\sqrt{\frac{\phi c_t k}{\pi \mu}}. \quad (19)$$

The leakoff coefficient can be generalized to include the effect of filtrate invasion and filtercake formation. Filtercake does not form during a DFIT because the injection is performed with water. Filtrate invasion is minor in DFIT's because of the low permeability and relatively large fracture surface area.

The G-function assumption of Carter leakoff is violated during a DFIT because pressure decreases over time (Castillo, 1987). As long as the change in the fracture pressure is relatively small relative to the difference between ISIP (initial shut-in pressure) and the formation fluid pressure, then the leakoff rate is reasonably described by Carter leakoff. But eventually, the fluid pressure drops sufficiently far that there is significant deviation from Carter leakoff (Castillo, 1987). The leakoff rate reduces relative to the rate that would have occurred if Carter leakoff had continued. Because $\frac{dV}{dG}$ is constant during Carter leakoff, the deviation causes $\frac{dV}{dG}$ to decrease (because leakoff occurs more slowly than if Carter leakoff had continued), and so the derivative of pressure with respect to G-time begins to decrease. This causes dP/dG to decrease and G*dP/dG to bend downward. The peaking of G*dP/dG and t*dP/dt occurs during the progressive transition from Carter leakoff to late-time impulse behavior (McClure, 2017).

A.5 The effect of closure

Equation 3 provides a conceptual framework for understanding the effect contact between the fracture walls. When the fracture walls come into contact, stiffness begins to increase (Equation 7). Increasing stiffness causes dP/dG to increase. Based on this insight, contact can be identified as occurring when dP/dG begins to increase (McClure et al., 2016).

Equation 3 depends on the assumption that pressure in the fracture can be described with a single parameter, *P*. This is valid if the fracture is approximately infinite conductivity. The dimensionless fracture conductivity is defined as:

$$C_{fD} = \frac{C_f}{0.5kL_f}, \quad (20)$$

where C_f is fracture conductivity and L_f is fracture length. Fractures are 'infinite conductivity' when C_{fD} is above approximately 300 (some authors use a lower threshold). From the cubic law, fracture conductivity is equal to (Witherspoon et al., 1980):

$$C_f = \frac{W^3}{12}. \quad (21)$$

For a fracture with half-length of 150 ft and matrix permeability of 100 nanodarcies, the fracture will be infinite conductivity as long as fracture aperture is greater than just 25 microns (equivalent to conductivity around 1 md-ft). Zhang et al. (2013) measured the conductivity of unpropped fractures in the Barnett Shale and found that conductivity remained above 1 md-ft until effective normal stress exceeded 1000s of psi. For unaligned fractures, the conductivity was even higher, and in-situ, fractures are probably rougher than in small-scale fractures induced in the lab.

For permeability on the order of microdarcies or millidarcies, it becomes less likely that the fracture will remain infinitely conductive after contact. If dimensionless fracture conductivity drops sufficiently rapidly with contact, then it is conceivable that nonnegligible pressure gradient could develop in the fracture. If this occurs, then contact would cause an apparent reduction in the 'leakoff rate,' $\frac{dV}{dG}$, and this could potentially cause the pressure derivative to decrease, rather than increase, with contact.

In the worst case, stiffness and leakoff rate could change in approximately equal amounts and result in no change in $\frac{dP}{dG}$ with contact. This scenario is probably uncommon because it requires coincidental equality of two opposing effects, but probably occurs occasionally. Decreasing $\frac{dP}{dG}$ with contact (due to decreased dimensionless fracture conductivity) has been confirmed by numerical simulation (McClure et al., 2016). If this occurred, $\frac{dP}{dG}$ may decrease monotonically after contact. If the fracture begins to become finite conductivity, it is possible that the conductivity could be spatially variable along the fracture area.

A.6. Impulse flow

Craig and Blasingame (2006) pointed out that the late time behavior of a DFIT can be described with impulse flow solutions from conventional well test analysis. The impulse flow solution can be found by taking the dimensionless time derivative of the nondimensionalized solution for constant-rate injection (Houze et al, 1988; Ayoub et al., 1988; Gu et al, 1993). For example, constant rate injection into an infinite conductivity fracture yields a scaling of $\Delta P \propto (\Delta t)^{\frac{1}{2}}$ (Gringarten et al., 1974). Therefore, the impulse solution for an infinite conductivity fracture is $\Delta P \propto (\Delta t)^{-\frac{1}{2}}$. Late-time impulse transients can be used to infer permeability and fluid pressure (Sections A.10.iii and 3.1.6).

A.7 Near-wellbore pressure drop

In field DFIT's in horizontal wells, there is usually always a period of rapid pressure drop immediately after shut-in. At very early time, this pressure drop is due to the end of wellbore and perforation friction (if the well is perforated). But subsequently, there can be a period of rapid pressure drop that may last tens of minutes or longer. During this time, pressure commonly drops by 1000s of psi. This behavior is apparent in most of the field data reviewed in this study.

Near-wellbore pressure drop can be modeled as a pressure difference between the wellbore and the fracture (Wright, 2000):

$$\Delta P_{nw} = C_{nw} Q^{\beta}, \quad (22)$$

where C_{nw} is a constant, Q is the volumetric flow rate from the well into the fracture, and β is an exponent (typically equal to 0.5).

After shut-in, flow at the wellhead is zero, but fluid continues to flow into the formation because of wellbore storage. The flow rate Q can be estimated as:

$$Q = C_w \frac{dP}{dt}. \quad (23)$$

ΔP_{nw} can be estimated from the equation:

$$\Delta P_{nw} \sim P - P_{eff}, \quad (24)$$

where P is the bottomhole pressure of the well and P_{eff} is the 'effective' pressure estimated by extrapolating back to G-time equal to zero from the point of minimum dP/dG (Section 3.1.1). P_{eff} is an estimate for the fluid pressure in the fracture, on the 'other side' of the near-wellbore pressure drop from the wellbore.

These relations make it possible to plot the difference between well pressure and fracture pressure versus volumetric flow rate and directly infer C_{nw}.

A.8 The h-function

Nolte (1979) derived the G-function to be proportional to the cumulative leakoff volume after shut-in and derived the g-function to be proportional to the total volume of fluid leaked off after the start of injection. Both functions are derived assuming Carter leakoff. Following a similar approach, it is convenient to define an 'h' function that is proportional to the cumulative leakoff volume from the start of injection, but unlike the g-function, accounts for deviation from Carter leakoff caused by pressure change over time. This is accomplished using a time-convolution integral of the one-dimensional constant pressure solution (given by Equation 18). This approach is related to the method described by Mayerhofer and Economides (1993) and Mayerhofer et al. (1995), who proposed a procedure for estimating permeability using an approximation to the leakoff rate and then a convolution integral of the constant rate solution (Section A.3.vii), and is also related to the relative stiffness relations developed by Wang and Sharma (2018).

The cumulative leakoff from the start of pumping can be estimated as:

$$V_L = 4A\sqrt{\frac{k\phi c_t}{\pi\mu}} \int_0^{\Delta t + t_e/2} \frac{(P(\tau) - P_{res})}{d\tau} \sqrt{\Delta t + t_e/2 - \tau}\, d\tau = 4Ah(\Delta t)\sqrt{\frac{k\phi c_t}{\pi\mu}}. \quad (25)$$

Thus, the h-function is defined as:

$$h(\Delta t) = \int_0^{\Delta t + t_e/2} \frac{(P(\tau) - P_{res})}{d\tau} \sqrt{\Delta t + t_e/2 - \tau}\, d\tau. \quad (26)$$

If pressure versus time is known, cumulative leakoff can be calculated as:

$$V_L(\Delta t_k) \approx 4A\sqrt{\frac{k\phi c_t}{\pi\mu}} \left[(P_0 - P_{res})\sqrt{\Delta t_k + \frac{t_e}{2}} + \sum_{i=1}^{k}(P_i - P_{i-1})\sqrt{\Delta t_k - \Delta t_i}\right]. \quad (27)$$

The h-function is calculated as:

$$h(\Delta t_k) \approx (P_0 - P_{res})\sqrt{\Delta t_k + \frac{t_e}{2}} + \sum_{i=1}^{k}(P_i - P_{i-1})\sqrt{\Delta t_k - \Delta t_i}. \quad (28)$$

Analogous to the G-function, an H-function can be defined that is proportional to the volume of fluid leaked off since shut-in:

$$H(\Delta t) = \int_{t_e/2}^{\Delta t + t_e/2} \frac{(P(\tau) - P_{res})}{d\tau} \sqrt{\Delta t + t_e/2 - \tau}\, d\tau. \quad (29)$$

The H-function is calculated as:

$$H(\Delta t_k) \approx (P_0 - P_{res})\left(\sqrt{\Delta t_k + \frac{t_e}{2}} - \sqrt{\frac{t_e}{2}}\right) + \sum_{i=1}^{k}(P_i - P_{i-1})\sqrt{\Delta t_k - \Delta t_i}. \quad (30)$$

Cumulative leakoff after shut-in can be written as:

$$V_{Ls}(\Delta t_k) \approx 4AH(\Delta t_k)\sqrt{\frac{k\phi c_t}{\pi\mu}}\,. \tag{31}$$

The h-function can be calculated directly from pressure versus time data and an estimate of the reservoir pressure, P_{res}. Estimation of reservoir pressure is discussed in Section 3.1.6.

Unlike the G-function, Equation 25 does not rigorously account for the effect of the propagation of the fracture over time. Instead, leakoff during injection is approximated by assuming the fracture formed instantaneously after a duration of injection of $t_e/2$. Although simple, this is a reasonably accurate approximation. Equation 25 implies that the volume of fluid leaked off at shut-in is equal to:

$$V_L(\Delta t = 0) \approx 4A\sqrt{\frac{k\phi c_t}{\pi\mu}}\left[(P_0 - P_{res})\sqrt{\frac{t_e}{2}}\right] = 2AC_L\sqrt{t_e}\,\sqrt{2}. \tag{32}$$

The factor $\sqrt{2}$ in Equation 32 is analogous to $g(\Delta t = 0) = g_0$ in Equation 13 (which is taken from the more detailed derivations of Nolte, 1979, and Gulrajani and Nolte, 2000). g_0 is bounded within the range 4/3 and $\frac{\pi}{2}$, and $\sqrt{2}$ lies within this range.

A.9 Relative stiffness

Using Equation 3 and Equation 25, it is possible to derive a 'relative stiffness' value (S_{rel}) that is linearly proportional to fracture stiffness:

$$\frac{dP}{dt} = \left(\frac{1}{C_t}\,\frac{dV}{dt}\right) \propto \frac{1}{C_t}\frac{dh}{dt}. \tag{33}$$

$$\frac{1}{C_t} \propto \frac{\frac{dP}{dt}}{\frac{dh}{dt}} = S_{rel}. \tag{34}$$

Using tabular data of pressure versus time and an estimate for formation fluid pressure, it is possible to directly calculate the relative stiffness:

$$S_{rel}(t_k) = \frac{\frac{dP}{dt}(t_k)}{\frac{dh}{dt}(t_k)} = \frac{dP(t_k)}{dh(t_k)}. \tag{35}$$

A plot of relative stiffness versus pressure can be used to identify contact. When the relative stiffness increases, this indicates that the fracture walls have come into contact (Wang and Sharma, 2018).

Because of near-wellbore pressure drop, the measured wellbore pressure after shut-in is typically higher than the actual pressure in the far-field fracture. To address this problem, the relative stiffness and the h-function can be calculated using an 'effective pressure,' P_{eff}, that represents a best estimate for the true pressure in the fracture (Section 3.1.1).

A.10 Methods of estimating permeability

The following sections describe methods for estimating permeability and leakoff coefficient. We recommend estimating permeability from multiple techniques: the G-function technique, the h-function technique, impulse linear, and/or impulse radial. These estimates use different parts of the data and can be compared for consistency. At the end of this section, we review several common methods that are not recommended.

A.10.i G-function technique

Combining with Equations 4 and 17:

$$\frac{dP}{dG} = \frac{1}{C_t}\,\frac{dV}{dG} = -\frac{\pi}{2}\,AC_L S_t\sqrt{t_e} = -\frac{\frac{\pi}{2}AC_L\sqrt{t_e}}{C_w + \frac{A}{S_f} + V_f c_{fl}}. \tag{36}$$

$\frac{dP}{dG}$ can be directly estimated from the data. $V_f c_{fl}$ is negligibly small and is omitted from the following equations. Assuming a radial crack, the leakoff coefficient can be calculated as:

$$C_L(radial) = -\frac{dP}{dG}\frac{C_w+\frac{16R_f^3}{3E'}}{\frac{\pi^2}{2}R_f^2\sqrt{t_e}} = -\frac{dP}{dg}\frac{C_w+\frac{16R_f^3}{3E'}}{2\pi R_f^2\sqrt{t_e}}. \quad (37)$$

Assuming a fixed-height (PKN) crack, the leakoff coefficient can be calculated as:

$$C_L(PKN) = -\frac{dP}{dG}\frac{\frac{2C_w}{\pi}+\frac{L_f h_f^2}{E'}}{L_f h_f\sqrt{t_e}} = -\frac{dP}{dg}\frac{2C_w+\frac{L_f h_f^2 \pi}{E'}}{4L_f h_f\sqrt{t_e}}. \quad (38)$$

Equations 37 and 38 cannot be solved directly because they require estimation of the fracture size, either radius or length. In addition, the PKN calculation requires an assumption of fracture height. It is not possible to estimate height solely from the DFIT. It needs to be estimated from ancillary information, such as knowledge of a stress contrast creating height confinement. If wellbore storage is neglected and height is assumed, Equation 38 reduces to an equation that can be solved directly for leakoff coefficient (Marongiu-Porcu et al., 2011).

Radius and length in Equations 37 and 38 can be estimated by writing a mass balance equation for the entire system:

$$V_{inj} = C_w\big(P(\Delta t) - P_{w,init}\big) + \frac{A}{S_f}(P(\Delta t) - Shmin) + 2AC_L\sqrt{t_e}g(\Delta t). \quad (39)$$

Equation 39 states that the volume of fluid injected is equal to wellbore storage, fluid stored in the fracture, and leakoff. Equation 39 forms a system of two equations (with Equation 37 or 38) and two unknowns (C_L and R_f or L_f). These equations can be solved to estimate leakoff coefficient and fracture extent. $P_{w,init}$ is the measured pressure at the beginning of injection. The term $C_w\big(P(\Delta t) - P_{w,init}\big)$ accounts for the net flow due to wellbore storage.

Equations 37, 38, and 39 must be evaluated at a particular point in time. We recommend evaluating dP/dG at the minimum point in dP/dG. Because dP/dG is never constant, this point is probably distorted by both near-wellbore pressure drop and contact. As a result, it is an *upper bound* on the true value of dP/dG and may lead to an overestimate of leakoff coefficient. Nevertheless, it is the best available point in time to estimate dP/dG.

We recommend evaluating Equation 39 at the effective ISIP (Section 3.1.1) in order to minimize the relative impact of the Shmin uncertainty on the calculation of net pressure. Equation 39 is evaluated from the estimate of the effective ISIP, rather than the literal ISIP, because near-wellbore pressure drop elevates the literal ISIP far above the actual pressure in the fracture at shut-in.

Once leakoff coefficient has been calculated, permeability can be calculated from Equation 19.

A.10.ii h-function technique

The assumption of Carter leakoff is a limitation of the G-function method. This limitation can be overcome using the h-function method. Similar to Equation 39, we can write a mass balance on the system using the h-function to calculate leakoff:

$$V_{inj} = C_w\big(P(\Delta t) - P_{w,init}\big) + \frac{A}{S_f}\,(P(\Delta t) - Shmin) + 4Ah(\Delta t)\sqrt{\frac{k\phi c_t}{\pi\mu}}\,. \quad (40)$$

After selecting appropriate values for A and S_f (for either radial or PKN geometry), Equation 40 contains two unknowns: permeability and fracture radius (or length). The problem is solved by evaluating the equation at two different points in time: at shut-in (using the effective ISIP) and at the point of maximum G*dP/dG. The point of maximum G*dP/dG is reached a significant period of time after the fracture walls

come into contact. The fracture still retains some aperture, but it is reasonable to assume that the great majority of fluid has leaked off from the system. Specifically, we assume that 10% of the total injection volume remains stored in the fracture at this point in time (the calculation is not strongly dependent on the precise percentage that is assumed). This assumption yields:

$$0.9V_{inj} = C_w\left(P_{peak} - P_{w,init}\right) + 4Ah(\Delta t_{peak})\sqrt{\frac{k\phi c_t}{\pi\mu}}\ . \quad (41)$$

Rearrangement yields an equation for $A\sqrt{k}$:

$$A\sqrt{k} = \frac{0.9V_{inj} - C_w\left(P_{peak} - P_{w,init}\right)}{4h(\Delta t_{peak})\sqrt{\frac{\phi c_t}{\pi\mu}}}. \quad (42)$$

Equation 40 can be solved for area:

$$A = \left(V_{inj} - C_w\left(P(\Delta t) - P_{w,init}\right) - A\sqrt{k}\left(4h(\Delta t)\sqrt{\frac{\phi c_t}{\pi\mu}}\right)\right)\frac{S_f}{P - Shmin}. \quad (43)$$

$A\sqrt{k}$ can be calculated from Equation 42 and plugged into Equation 43. Appropriate relations for A and S_f are plugged into Equation 43, assuming either radial or PKN geometry, and the equation can be solved for either radius or fracture length. Then, it is trivial to calculate area and permeability.

We recommend evaluating Equation 40 at Δt equal to zero (using the effective ISIP) in order to minimize the relative effect of uncertainty in the estimate of Shmin. For the case of $\Delta t = 0$, Equation 40 reduces to:

$$V_{inj} = C_w\left(P_{ISIP,eff} - P_{w,init}\right) + 4(A\sqrt{k})\left(P_{ISIP,eff} - P_{res}\right)\sqrt{\frac{t_e}{2}}\sqrt{\frac{\phi c_t}{\pi\mu}} + \frac{A}{S_f}\left(P_{ISIP,eff} - Shmin\right). \quad (44)$$

For radial geometry, the radius is calculated as:

$$R_f = \sqrt[3]{\frac{3E'\left[V_{inj} - C_w\left(P_{ISIP,eff} - P_{w,init}\right) - 4\left(A\sqrt{k}\right)\left(P_{ISIP,eff} - P_{res}\right)\sqrt{\frac{t_e}{2}}\sqrt{\frac{\phi c_t}{\pi\mu}}\right]}{16\left(P_{ISIP,eff} - Shmin\right)}} \quad (45)$$

For PKN geometry, the fracture length is calculated as:

$$L_f = \frac{2E'\left[V_{inj} - C_w\left(P_{ISIP,eff} - P_{w,init}\right) - 4\left(A\sqrt{k}\right)\left(P_{ISIP,eff} - P_{res}\right)\sqrt{\frac{t_e}{2}}\sqrt{\frac{\phi c_t}{\pi\mu}}\right]}{h_f^2\pi\left(P_{ISIP,eff} - Shmin\right)}. \quad (46)$$

A.10.iii Impulse linear

The late time behavior of a DFIT can be interpreted like an impulse test from classical well test analysis (Craig and Blasingame, 2006). The late-time analytical solution for linear flow with constant rate injection is (Gringarten et al., 1974):

$$P = P_{res} + \frac{Q}{A}\sqrt{\frac{\mu}{\pi k c_t \phi}}\sqrt{\Delta t}, \quad (47)$$

where Q is the volumetric injection rate. Taking the derivative of the nondimensionalized form of the equation, we can find the solution for injection of a volume of fluid V_{slug} into the system (Houze et al, 1988; Ayoub et al., 1988; Gu et al, 1993). V_{slug} should take wellbore storage into account:

$$P = P_{res} + \frac{V_{inj} - C_w\left(P_{res} - P_{w,init}\right)}{2A}\sqrt{\frac{\mu}{\pi k c_t \phi}}\frac{1}{\sqrt{\Delta t}}. \quad (48)$$

Equation 48 can be rearranged to calculate $A\sqrt{k}$ from the slope of a plot of pressure versus $\frac{1}{\Delta t^{1/2}}$. Once $A\sqrt{k}$ has been estimated, radius (or length) and permeability can be estimated from Equations 45 and 46.

A.10.iv Impulse radial

The late-time analytical solution for radial flow with constant rate injection is (Theis, 1935; Horne, 1995):

$$P - P_{res} = \frac{Q\mu}{2\pi kh}[0.5\left(ln\left(\frac{k\Delta t}{\phi\mu c_t r_w^2}\right) + 0.80907\right) + s]. \quad (49)$$

Therefore, impulse radial is the derivative of the constant rate solution (Houze et al, 1988; Ayoub et al., 1988; Gu et al, 1993):

$$P - P_{res} = \frac{(V_{inj} - C_w(P_{res} - P_{w,init}))\mu}{4\pi kh}\frac{1}{\Delta t}. \quad (50)$$

Equation 50 can be rearranged to show that the permeability-thickness product, kh, can be calculated from the slope of a plot of pressure versus $\frac{1}{\Delta t}$. To calculate permeability, it is necessary to make an estimate for *h*, the height of the permeable formation. If well logs indicate that there is a clear 'pay' zone with higher permeability than surrounding formations, then the thickness of this zone can be used for *h*. Alternatively, if well logs indicate strong height confinement, then the fracture can be assumed to have known height, and this value can be used for *h*.

If there is not clear indication of height confinement and there is a not a single 'high permeability' pay zone, we recommend using a radial fracture geometry and setting *h* equal to $2R_f$. For known *kh* (estimated from Equation 50), then *k* is approximately equal to $\frac{(kh)_{est}}{2R_f}$. Equation 44 becomes:

$$V_{inj} = C_w(P_{ISIP,eff} - P_{w,init}) + 4\left(\pi R_f^2\sqrt{\frac{(kh)_{est}}{2R_f}}\right)(P_{ISIP,eff} - P_{res})\sqrt{\frac{t_e}{2}}\sqrt{\frac{\phi c_t}{\pi\mu}} + \frac{16R_f^3}{3E'}(P_{ISIP,eff} - Shmin) \quad (51)$$

Equation 51 is a cubic equation for R_f. It can be solved with a nonlinear solver and then used to estimate *h* and *k*.

A.11 The linear flow time function

Sometimes, impulse interpretations are performed with the 'linear flow time function' defined by Gulrajani and Nolte (2000) as:

$$F_L = \frac{2}{\pi}\sin^{-1}\sqrt{\frac{t_c}{\Delta t}}, \quad (52)$$

where t_c is the shut-in time to 'closure.' F_L is only defined for $\Delta t \geq t_c$. $A\sqrt{k}$ is estimated from impulse linear flow using a plot of pressure versus F_L or F_L^{-1}. kh is estimated from impulse radial flow using a plot of pressure versus F_L^2 or F_L^{-2}.

Equation 52 can be understood by considering the behavior of the arcsine function as its argument approaches zero:

$$\lim_{x\to 0}\sin^{-1} x = x. \quad (53)$$

Therefore, once $t_c + \Delta t$ is substantially larger than t_c, F_L can be approximated as:

$$F_L \approx \frac{2}{\pi}\sqrt{\frac{t_c}{\Delta t}}. \quad (54)$$

For Δt equal to $2t_c$, the approximation is accurate within 11%. For Δt equal to $10t_c$, the approximation is accurate within 2%.

Thus, for most practical purposes, a plot of pressure versus F_L is equivalent to a plot of pressure versus reciprocal square root of time, and a plot of pressure versus F_L^2 is equivalent to a plot of pressure versus reciprocal time. A plot of F_L^{-2} is equivalent to a plot of pressure versus time.

The F_L function is significantly different from $\frac{2}{\pi}\sqrt{\frac{t_c}{\Delta t}}$ in the period from $\Delta t = t_c$ to $\Delta t = 2t_c$ (it is not defined prior to t_c). Should F_L be used if data is not available for Δt greater than $2t_c$? Possibly, but interpreters should keep in mind the assumptions underlying F_L. It is derived assuming that Carter leakoff occurs until closure, and then there is zero leakoff after closure (Nolte et al., 1997; page 76 from Carslaw and Jaeger, 1959). But in reality, leakoff rate gradually deviates from Carter leakoff as pressure decreases in a system coupled with nonlinear evolution of system storage (Section A.13). Because of this simplification, the period from $\Delta t = t_c$ to $\Delta t = 2t_c$ is the period when the assumptions underlying F_L are least reliable. After this period, F_L is similar to the impulse solution.

A.12 Estimating efficiency

Fracture efficiency, η, is defined as the volume of fluid remaining in the fracture at shut-in divided by the volume of fluid injected into the fracture (the total injection volume minus wellbore storage). A classical equation for estimating efficiency is (Equation 9-60 from Gulrajani and Nolte, 2001):

$$\eta = \frac{G_c}{2+G_c}, \tag{55}$$

where G_c is G-time at 'closure.'

Equation 55 is derived assuming the same assumptions discussed in Section A.11: Carter leakoff occurs until 'closure,' at which point there is zero fluid remaining in the fracture. Conventionally, Equation 55 would be applied with the tangent method for picking closure. But there has been substantial deviation from Carter leakoff by the time of the tangent closure pick. As discussed in Section 3.1.9, due to fracture roughness, there is likely to be significant fluid remaining the fracture at the point of contact, and even when pressure is equal to or less than Shmin. Because of the offsetting effect of different approximations, Equation 55 often yields a reasonable approximation of efficiency in many cases if applied with the tangent method of picking closure.

Alternatively, efficiency can be estimated after estimating leakoff coefficient and/or permeability using the techniques in Section A.10. Then, cumulative leakoff at shut-in can be estimated from Equation 13, and efficiency can be calculated directly by applying mass balance (including the effect of wellbore storage):

$$\eta = \frac{V_{inj} - C_w\left(P - P_{w,init}\right) - V_L(\Delta t=0)}{V_{inj} - C_w(P - P_{w,init})}. \tag{56}$$

A.13 Estimating pore pressure with a short shut-in

Sometimes, DFIT's are not performed with sufficient shut-in duration to reach impulse linear or radial. A simple numerical simulation and history match can be used to provide a rough estimate for fluid pressure.

1. Assume W_0 and P_{res}.
2. Use the h-function method to integrate the measured pressure data (after conversion to P_{eff}) and use the method in Section A.10.ii to infer leakoff coefficient and fracture surface area. Use the estimated area and assumed fracture geometry to calculate $S_{f,o}$.
3. Numerically solve the following equation for a DFIT pressure transient (derived from Equation 3):

$$\frac{dP}{dt}\left(\frac{A}{S_f} + C_w\right) = \frac{dV_L}{dt}. \tag{57}$$

$\frac{dV_L}{dt}$ is the leakoff rate, calculated from Equation 25. When the calculated aperture reaches W_o, the fracture stiffness is increased to account for the contribution of $S_{f,c}$, as discussed in Section A.1.ii. The integration can be solved numerically with explicit Euler:

$$P_k = P_{k-1} + \left(\frac{dP}{dt}\right)_k \Delta t, \tag{58}$$

where $\left(\frac{dP}{dt}\right)_k$ is calculated from Equation 57.

4. Check to see if the timing and value of the peak in t*dP/dt has been accurately predicted. If not, go back to Step 1 and select new values for W_0 and P_{res}. Iterate until convergence.

A.14 Generating plots of aperture versus effective normal stress

Wang and Sharma (2018) propose a method for estimating aperture versus pressure. The technique in this section is conceptually similar. From Equation 35, the derivative of *P* with respect to *h* is proportional to system stiffness. Therefore, neglecting wellbore storage, we can write:

$$\frac{\frac{dP}{dh}}{(\frac{dP}{dh})_{min}} \frac{S_f}{A} = \frac{dP}{dV}. \tag{59}$$

The permeability estimation methods in Section A.10 yield estimates of fracture area and stiffness prior to contact, S_{fo}. Next, estimate the derivative of pressure with respect to aperture:

$$\frac{dP}{dW} = A\frac{dP}{dV}. \tag{60}$$

If we assume that aperture at the peak of G*dP/dG is an arbitrary, small value, 3.28e-5 ft, then we can perform an integral to roughly approximate average fracture aperture as a function of pressure:

$$W(P) = 3.28 * 10^{-5} + \int_{P_{pG}}^{P} \frac{1}{\frac{dP}{dW}} dP, \tag{61}$$

where P_{pG} is the pressure at the peak G*dP/dG. Figure 7 shows a result from this procedure.